P-Site Structural Diversity and Evolution in a Zeosil Catalyst

Sheetal K. Jain,[†,‡] Tarnuma Tabassum,[†,‡] Li Li,[†] Limin Ren,[#,⊥] Wei Fan,[°] Michael Tsapatsis,[||,∇] Stavros Caratzoulas,[^] Songi Han,[†,§,*] Susannah L. Scott[†,§,*]

[†] Department of Chemistry & Biochemistry, University of California, Santa Barbara, CA 93106, United States

[#] Department of Chemical Engineering and Materials Science, University of Minnesota, 421 Washington Ave SE, Minneapolis, MN 55455, United States

[°] Department of Chemical Engineering, University of Massachusetts Amherst, 686 N Pleasant St, Amherst, MA 01003 United States

[^] Delaware Energy Institute, 221 Academy Street, Newark, DE 19716, United States

[||] Department of Chemical and Biomolecular Engineering and Institute for NanoBiotechnology, Johns Hopkins University, 3400 N. Charles Street, Baltimore, MD, 21218 United States

[∇] Applied Physics Laboratory, Johns Hopkins University, 11100 Johns Hopkins Road, Laurel, MD 20723, United States

[§] Department of Chemical Engineering, University of California, Santa Barbara, CA 93106, United States

KEYWORDS P-zeosil, Brønsted Acidity, Hydrolysis, Acid Catalysis, Frequency-selective solid-state NMR, DFT

ABSTRACT: Phosphorus-modified siliceous zeolites, or P-zeosils, catalyze the selective dehydration of biomass derivatives to platform chemicals such as *p*-xylene and 1,3-butadiene. Water generated during these reactions is a critical factor in catalytic activity, but the effects of hydrolysis on the structure, acidity, and distribution of the active sites are largely unknown. In this study, the P-sites in an all-silica self-pillared pentasil (P-SPP) with a low P-loading (Si/P = 27) were identified by solid-state ^{31}P NMR using frequency-selective detection. This technique resolves overlapping signals for P-sites that are covalently bound to the solid phase, as well as oligomers confined in the zeolite but not attached to the zeolite. The sensitivity necessary to conduct ^{29}Si-filtered ^{31}P detection and ^{31}P-^{31}P correlation experiments was achieved using dynamic nuclear polarization. These techniques distinguish sites with P-O-Si linkages from those with P-O-P linkages. The spectra reveal a previously unappreciated diversity of P-sites, including evidence for surface-bound oligomers. In the dry P-zeosils, essentially all P-sites are anchored to the solid phase, including mononuclear sites and dinuclear sites containing the [Si-O-P-O-P-O-Si] motif. The fully condensed sites evolve rapidly when exposed to humidity, even at room temperature. Hydrolysis generates more species with a wide range of acidities, inferred from their calculated LUMO energies. Initial cleavage of some P-O-Si linkages results in an evolving mixture of surface-bound mono- and oligo-nuclear P-sites with increased acidity. Subsequent P-O-P cleavage leads to a decrease in acidity as the P-sites are eventually converted to H_3PO_4. The ability to identify the acidic sites in P-zeosils and describe their structure and stability will play an important role in regulating the water content to control activity in microporous catalysts.

INTRODUCTION

Robust catalysts that can transform lignocellulose into fuels and chemicals will be needed to shift chemical manufacturing towards the use of biomass as a source of renewable carbon. Aluminosilicate zeolites are already well-established as catalysts for the conversion of fossil carbon due to their high acidity and stability, and they are poised to play similar roles for biomass-derived carbon.[1,2] However, these zeolites are rapidly deactivated by side-products formed in unselective reactions of biomass intermediates. One approach to improve the selectivity of these catalysts, and thereby enhance their stability, is to attenuate their strong acidity. Moderate Brønsted acidity can be installed in siliceous zeolites by infusing them with orthophosphoric acid (H_3PO_4). Confinement of the acid in these microporous materials may also confer shape-selectivity.[3] The resulting P-zeosils are related compositionally to amorphous H_3PO_4-modified silicas, known as "solid phosphoric acids" (SPAs). The SPAs have been used commercially since the 1930s in large-scale catalytic processes such as propene oligomerization and benzene alkylation.[4–6] Recently, an SPA was also reported to steer the fast pyrolysis of cellulose toward levoglucosenone.[7,8] The active sites in SPAs are suggested to be free phosphoric acid oligomers, whose proximity to the silica surface shifts the oligomerization equilibria and alters the catalytic activity. Introducing phosphorus also changes the acidity of crystalline aluminosilicates,[9–12] and is widely used to improve zeolite stability under hydrothermal reaction conditions.[13] Yet despite decades of study, it is still unclear whether the catalytic activity of P-modified silicas and zeolites is due to free H_3PO_4, various polyphosphoric acid oligomers, or P-sites covalently bonded to the solid phase.

Recently, a self-pillared pentasil (SPP) and a dealuminated Beta (BEA) zeolite, both modified with phosphorus, were reported to catalyze two noteworthy reactions: the Diels-Alder coupling of carbohydrate-derived 2,5-dimethylfuran with ethylene to give *p*-xylene, and the tandem dehydration-ring opening of tetrahydrofuran to give 1,3-butadiene.[14,15] Both zeosils are all-silica materials (i.e., containing

no aluminum) and, in the absence of phosphorus, show no activity for either reaction. Their enhanced activity and selectivity relative to H_3PO_4 was attributed to surface-bound P-sites,[14] although the existence of such sites was not established. Surface and/or pore confinement in a siliceous material could promote H_3PO_4 condensation with itself and/or the silica framework, leading to formation of P-O-P and/or P-O-Si linkages.[16] Describing the environment-dependent speciation of these P-sites is a necessary first step towards establishing structure-activity relationships for P-based solid acid catalysts.

X-ray diffraction (XRD) cannot be used to study structures of P-sites in amorphous materials, or the disordered phases of semi-crystalline materials like P-modified aluminum (hydro)oxides and P-zeosils. However, total X-ray scattering has recently been applied to the structural analysis of adsorbed (poly)phosphates, through analysis of the differential pair-distribution function. The findings suggest the formation of surface-bound complexes, although the ability to resolve structural information when multiple sites are present is low.[17–19] The sites in P-containing silica glasses, aluminophosphate and aluminosilicate molecular sieves, as well as silicophosphates, have been probed using a variety of spectroscopic techniques.[20] In principle, the presence of P-O-Si and P-O-P linkages can be confirmed by their characteristic IR[21–23] and Raman vibrations,[24,25] but here too precise assignments are elusive in the presence of multiple types of P and Si species. Linear combination analysis of the P K-edge XANES suggested the formation of various adsorbed (poly)phosphates on γ-Al_2O_3.[26] Shifts in the P $L_{2,3}$-edge XANES were correlated with polyphosphate chain length in SiO_2-P_2O_5 and Na_2O-SiO_2-P_2O_5 glasses,[27] but the presence of P-O-Si linkages could not be confirmed. Various computational studies reached inconsistent conclusions regarding the thermodynamic stabilities of such linkages in different materials.[28,29] To-date, there are no comparable studies on P-zeosils.

Solid-state NMR spectroscopy is a powerful way to probe the nature of P-sites directly, and can be used to study both crystalline and amorphous materials. In particular, ^{31}P Magic-Angle Spinning NMR (MAS-NMR) has been used extensively to investigate silicophosphate gels/glasses,[30–32] SPA catalysts,[33] phosphates adsorbed on aluminum (hydr)oxides,[17,26] and partially dealuminated P-modified aluminosilicate zeolites.[13] Replacement of H by Si gives rise to surface-bound P-sites with structures described as $O=P(OH)_2(OSi)$, $O=P(OH)(OSi)_2$, and $O=P(OSi)_3$. The last member of the series, $P(OSi)_4$, is observed in crystalline silicophosphate phases. Adopting a nomenclature conventionally used for ^{29}Si NMR signals, the anchored P-sites are labeled Q^n, where n denotes the number of Si next-nearest neighbors (i.e., P-O-Si linkages).

In aqueous solution, H_3PO_4 exists in concentration-dependent equilibria with several linear and cyclic oligomers, including pyrophosphoric acid ($H_4P_2O_7$), acyclic tripolyphosphoric acid ($H_5P_3O_{10}$), and cyclic metaphosphoric acid ($H_3P_3O_9$).[34,35] Acyclic oligomers with the general formula $H_{m+2}P_mO_{3m+1}$ dominate the distribution.[34–36] They have been identified in the literature using a P^m nomenclature,[37] where m denotes the degree of oligomerization. The characteristic ^{31}P NMR signals for H_3PO_4 (P^1) and $H_4P_2O_7$ (P^2) appear at 0 and -12 ppm, respectively.[33] Trimetaphosphoric acid (P^3) has a single type of P-site with a chemical shift of -22 ppm,[38] while tripolyphosphoric acid has one internal and two terminal P-sites, with chemical shifts similar to those of trimetaphosphoric and pyrophosphoric acids, respectively.[33] Solid, fully condensed P_4O_{10} (phosphoric anhydride, P^4) gives rise to a signal at -46 ppm.[39]

Scheme 1 depicts the overlap of the ^{31}P NMR chemical shift ranges for Q^n sites with those of the corresponding P^{n+1} sites.[30,31] For amorphous siliceous materials, assignments are further complicated by the low ^{31}P NMR spectral resolution. These materials generally show fast nuclear spin relaxation arising from inhomogeneity in the local magnetic fields of the ^{31}P nuclei, dipolar interactions, and large ^{31}P chemical shift anisotropies (CSAs). The size of the CSAs relative to the MAS frequency also results in strong spinning sidebands that make the crowded ^{31}P NMR spectra more difficult to analyze. For sites with the same total number of Y substituents (Y = P or Si), but different chemical identities for Y (e.g., $O=P(OH)_2(OSi)$, Q^1, vs. $H_4P_2O_7$, P^2), it is usually impossible to assign a signal to a particular P-site based on its chemical shift alone. Precise identification of oligomers with P-O-P linkages, or surface-anchored sites with Si-O-P linkages, or mixed sites that contain both types of linkages,[40] remains an unsolved problem. Indeed, framework-anchored sites in siliceous materials have yet to be observed experimentally. Yet the ability to distinguish them is necessary to describe, model, and eventually tune the catalytic activity of P-modified materials.

Scheme 1. Structures of typical Q^n sites and their reported chemical shift ranges[14,31,40–48] (colored horizontal bars), as well as P^m sites and their discrete chemical shifts[33,38,39] (black vertical bars within each chemical shift range). The labels follow the principal naming conventions found in the literature for solid phases (Q^n) and aqueous solutions (P^m).

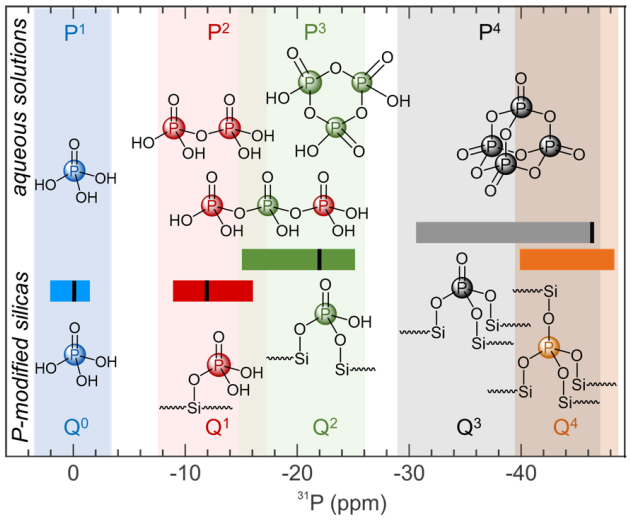

For crystalline siliceous materials, the presence and relative abundance of P-O-P and P-O-Si linkages can be established using multi-dimensional NMR experiments. For example, P-O-Si linkages in crystalline silicophosphates were observed using J-coupling-based 2D ^{29}Si-^{31}P NMR correlation spectroscopy.[32,49] Interactions *between* P-sites were assessed by ^{31}P-^{31}P correlation experiments, which probe through-bond (J-) or through-space (D-) coupling.[50–53] Unfortunately, J-coupling based approaches are not readily applied to the characterization of disordered P-sites in P-zeosils, due to the rapid relaxation of the ^{31}P and ^{29}Si nuclear spin coherence. Instead, the nature of the linkages in such materials must be demonstrated

using techniques based on *D*-coupling. Such multi-dimensional experiments involving ^{31}P or ^{29}Si are very challenging for dilute P-zeosils, due to the inherently low NMR sensitivity and low receptivity of ^{29}Si (4.7% natural abundance, with a gyromagnetic ratio only 20 % that of ^{1}H).

Recent advances in NMR that overcome its inherently low sensitivity are generating new opportunities for characterizing connectivities between ^{31}P and ^{29}Si nuclear spins. In particular, Dynamic Nuclear Polarization (DNP) can boost the sensitivity of MAS-NMR by several orders of magnitude,[54] making it possible to conduct multi-dimensional solid-state NMR studies of siliceous materials even with natural abundance ^{29}Si. Specifically, ^{29}Si-^{31}P and ^{31}P-^{31}P correlation experiments can be performed using DNP-enhanced MAS NMR with reasonable experimental times (a few hours). In this study, DNP-enhanced MAS-NMR spectroscopy was combined with advanced NMR pulse sequences to identify the P-sites present in a P-zeosil.

P-modified SPP, with an atomic ratio Si/P of 27, is a meso/microporous Mobil Five (MFI)-type zeolite. Consisting of orthogonally-intergrown single unit-cell MFI nanosheets (Scheme 2), it is hydrothermally stable at moderate temperatures.[55–57] Its framework encompasses both conventional MFI micropores located within the 2 nm-thick nanosheets, as well as mesopores formed between the intergrown nanosheets and defined by the external surfaces of the MFI nanosheets, which are mostly terminated by (010) planes. The material shows a rich P-speciation, which depends strongly on the extent of hydration. We aim to identify the surface-bound and near-surface phosphoric acid oligomers and monomers, including those in which P-O-P and P-O-Si linkages are present simultaneously in the same P-sites.

Scheme 2. Transmission electron microscopy image of a typical Self-Pillared Pentasil (SPP) particle (left), consisting of orthogonally-intergrown MFI nanosheets of single-unit-cell (2 nm) thickness, and a schematic of the basic unit, showing two 2 nm-thick intergrown MFI nanosheets (right).

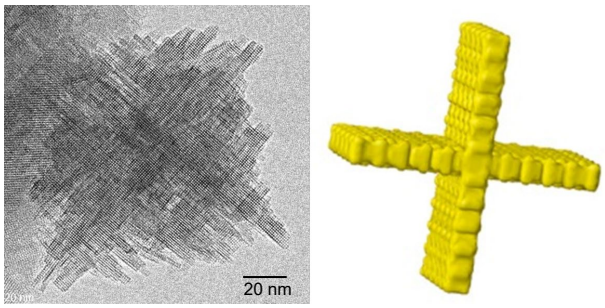

RESULTS AND DISCUSSION

Describing the P-sites in dry P-SPP. To explore the P-sites present in the absence of water, P-SPP (Si/P = 27) was dried *in vacuo* at 450 °C. Its 1D ^{31}P MAS NMR spectrum was recorded without exposure of the dry material to air, using direct excitation at 18.8 T (Figure 1a). The spectrum consists predominantly of an isotropic peak at -44 ppm and its spinning sideband at 21 ppm, confirmed by comparison to the simulation in Figure 1a. According to Scheme 1, it is either a P^4 or a Q^3 signal. From this point forward, we will use only the Q^n-nomenclature for simplicity.

The chemical shift anisotropy (CSA), also obtained from the simulation of the ^{31}P MAS NMR spectrum, is (-205 ±29) ppm (i.e., 66 ± 9 kHz at 18.8 T, Table S1). The linewidth, ca. 3.5 kHz at ν_r = 20 kHz, suggests that it is dominated by isotropic chemical shift dispersion, arising from the superposition of multiple, structurally heterogeneous P-sites with distinct isotropic chemical shifts. Such sites may include surface-bound $O{=}P(OSi)_3$, non-surface-bound P_4O_{10}, and components of more complex mixed sites. Although the broad Q^3 signal and its spinning sidebands are the dominant spectral features, minor Q^n signals ($n \neq 3$) may also be present, and could account for the additional signal intensity not predicted by the simulated spinning sidebands of the Q^3 signal. However, the poor spectral resolution and low signal-to-noise ratio (SNR) preclude more definitive characterization of the material on the basis of this spectrum alone.

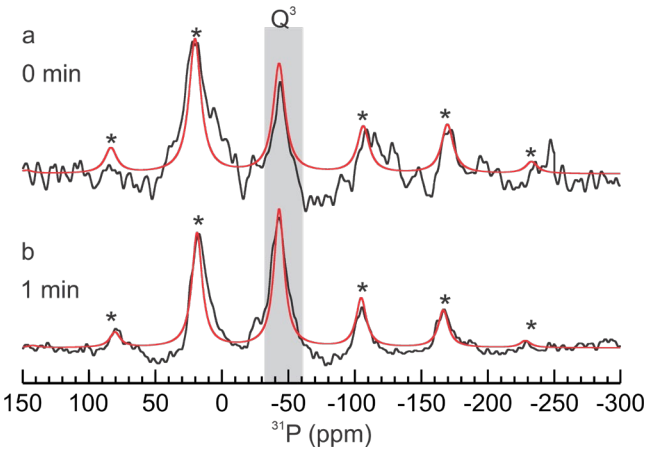

Figure 1. ^{31}P MAS-NMR spectra (black) of P-SPP (Si/P = 27), in (a) its fully dry state (i.e., 0 min ambient exposure), and (b) after 1 min exposure to the laboratory ambient. Both spectra were recorded at room temperature and 18.8 T, with 20 kHz MAS and a 5s repetition delay. The number of scans for the dry and 1 min air-exposed samples was 1024 and 256, respectively. Asterisks indicate spinning sidebands. Simulations (red) were performed using the CSA model in Topspin 4.0.6.

Many catalytic reactions involving biomass are conducted in the presence of water, and/or generate water as a by-product. Since previous studies of SPA[4,36,58] and P-modified zeolites[59] show that both P-speciation and/or activity are very sensitive to the hydration state, we investigated the effect of water on the P-site distribution in the P-zeosil. The ^{31}P NMR spectrum of dry P-SPP was recorded again after removing the rotor cap to effect a brief (ca. 1 min) air exposure at room temperature in the laboratory ambient (we will refer to this operation as "ambient exposure" throughout the rest of the paper). Although the chemical shift of the major isotropic peak at -44 ppm did not change, another small, isotropic peak became clearly apparent at -25 ppm (Figure 1b). Its chemical shift is typical of a Q^2 signal. At the same time, the absolute area of the NMR spectrum increased by a factor of 10 and the SNR increased 12-fold, resulting in a better-resolved sideband pattern. The higher NMR sensitivity in this minimally hydrolyzed state reflects a reduced CSA, (-160 ± 9) ppm,

compared to (-205 ± 29) ppm for the dry material. This change leads to increased efficiency of the RF excitation.

Since the CSA values are larger than the RF amplitude (~35 kHz) used for the excitation pulse, the appearance of the spinning sideband manifold may be distorted by the non-uniform excitation, increasing the uncertainties in the CSA parameters (see Table S1). Nevertheless, the changes in the overall spectral intensity and sideband patterns confirm a reduction in CSA after just 1 min ambient exposure (see Figure S1). The reduction in CSA occurs concurrently with a decrease in linewidth of the isotropic Q^3 peak, from 3.5 to 3.0 kHz. This indicates that the isotropic chemical shift dispersion is also lower in ambient air-exposed P-SPP. These observations are consistent with an increase in average mobility and/or a reduced structural heterogeneity of the P-sites relative to the fully dry state.

Gradual changes in P speciation upon exposure to moisture. The extent of P-zeosil hydration was increased by prolonging the ambient exposure (by removing the NMR rotor cap for longer times). The resulting changes in P speciation were observed by ^{31}P NMR (Figure 2a). After 4 min ambient exposure, the peak at -25 ppm became more intense and a new peak appeared at -11 ppm. These signals correspond to chemical shifts in the Q^2 and Q^1 ranges, respectively. Thus, exposure to a very small amount of water vapor for even a brief duration (4 min) is sufficient to convert some of the P-sites with signals in the Q^3 region to new P-sites. After further ambient exposure (9 min), four distinct groups of signals are present

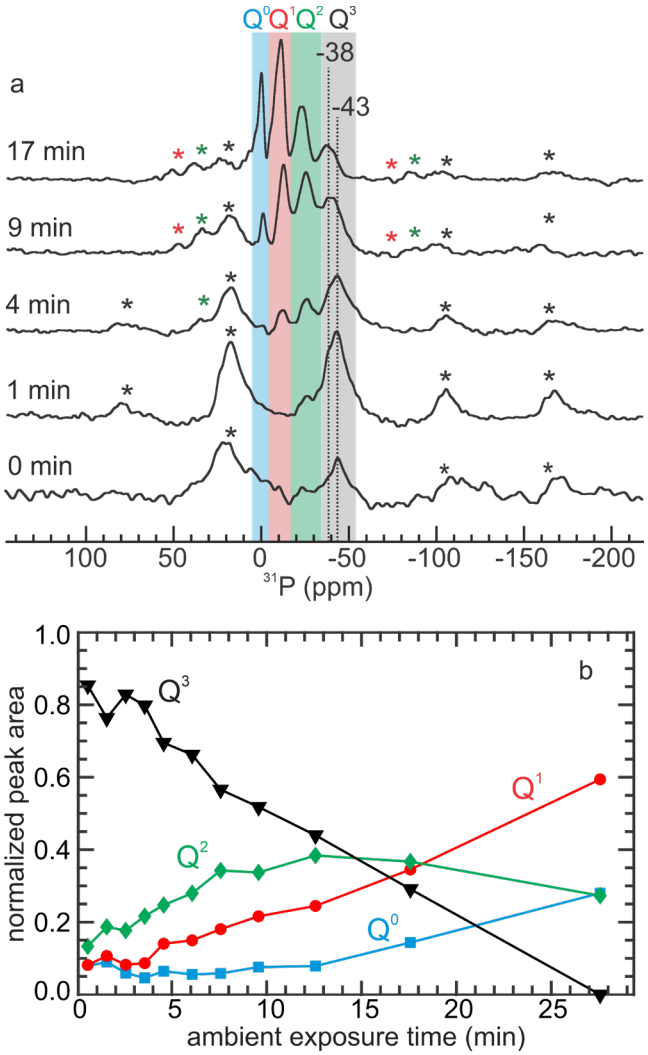

Figure 2. The effect of ambient exposure time (correlated approximately with the amount of adsorbed water) at room temperature, on the P speciation in P-SPP: (a) ^{31}P MAS NMR spectra recorded after each ambient exposure time, as noted. All spectra were recorded at room temperature in an 18.8 T magnet using 20 kHz MAS. Spinning sidebands for Q^1, Q^2, and Q^3 signals are indicated by * in red, green, and black, respectively. (b) Approximate time profile of the integrated peak intensities (including spinning sidebands) for each group of Q^n signals.

(Q^n, where n = 0-3), including a new peak at 0 ppm (Q^0) assigned to H_3PO_4. A second isotropic Q^3 peak at -38 ppm emerges, distinct from spinning sidebands. The spinning sidebands become successively less intense and all peaks narrow as the extent of hydration increases, presumably due to higher mobility and/or greater homogeneity in the remaining P-site structures.

Trends in the various Q^n peak areas with ambient exposure time (Figure 2b) reflect on the relative hydrolytic stabilities of each group of P-sites (spectra for all ambient exposure times are shown in Figure S2). The Q^3 signals, which dominate the spectrum of the dry material, decrease gradually in intensity, disappearing completely after ca. 25 min. Over the same time period, the Q^2 signal intensity first increases and then decreases, suggesting that hydrolysis of some P-sites, initially responsible for Q^3 signals gives new sites with Q^2 signals. The intensities of the Q^1 and Q^0 signals increase monotonically,

but only after an induction period (which is shorter for Q^1 than for Q^0). The P-sites responsible for these two groups of signals must therefore be mostly secondary hydrolysis products, formed from P-sites associated with the Q^2 signals (although some could be formed directly by hydrolysis of the more stable sites associated with Q^3 signals). A ^{31}P NMR spectrum recorded after many days of ambient exposure (Figure S3) shows that most P-sites are eventually converted to H_3PO_4 (responsible for the Q^0 signal), while only a small residual Q^1 signal remains. Thus, the sensitivity to hydrolysis of the various groups of P-sites follows the general (and expected) order $Q^3 > Q^2 > Q^1$.

Overall, NMR measurements in the presence of variable water content reveal that multiple types of P-sites, with different sensitivities to water, coexist in partly hydrolyzed P-SPP. Under reaction conditions, P-SPP is neither completely dry nor fully hydrolysed, hence a distribution of P-sites with different Q^n signals will be present. More insightful methods are needed to assess the nature of these P-sites, in particular, the identities of the sites responsible for the different Q^3 signals, and whether any of the sites are surface-bound (via P-O-Si linkages).

Resolving P-speciation using DNP-enhanced MAS NMR. In principle, overlapping signals arising due to P-sites with either P-O-P or P-O-Si linkages can be distinguished via their ^{31}P-^{31}P and ^{31}P-^{29}Si correlations. However, conventional 1D ^{31}P MAS-NMR spectra such as those shown in Figure 1 already require tens of minutes of acquisition times (78 min for the fully dry material, and 22 min after 1-min ambient exposure). Hence, several days would be required to conduct the corresponding 2D measurements. Dynamic Nuclear Polarization (DNP) enhances NMR sensitivity dramatically by transferring electron spin polarization from a paramagnetic polarizing agent such as the TEKPOL biradical to solvent protons, and then (by cross-polarization) to ^{31}P nuclei. The resulting signal enhancements shorten the times required for ^{31}P-^{29}Si and ^{31}P-^{31}P correlation experiments significantly, and also facilitate the selective 1D detection of the various Q^n signals.

The DNP-enhanced ^{1}H-^{31}P CP-MAS spectrum of nearly-dry P-SPP shown in Figure 3a (recorded after ambient exposure time of ca. 2 min) could be acquired in less than 1 min using a ramped-CP pulse sequence (see Methods). The spectrum has a much higher SNR than a spectrum of the same material recorded for 22 min without DNP (i.e., with the microwave source turned off, see Figure S4 for comparison). The DNP-enhanced spectrum exhibits two major isotropic peaks, at -42 and -25 ppm, both with intense spinning sidebands. Based on their chemical shifts, these isotropic peaks correspond to P-sites with Q^3 and Q^2 signals, respectively. In contrast to the ^{31}P MAS-NMR spectrum in Figure 2a, the intensities of both signals are similar. ^{1}H-^{31}P CP detection is expected to enhance the Q^2 signal intensity relative to Q^3 , since the abundance of nearby ^{1}H should be higher for sites that give rise to Q^2 signals (Scheme 1). The spinning sidebands are also stronger in Figure 3a compared to Figure 2a. This is a consequence of the slower MAS rate in the DNP experiment (7 kHz, vs. 20 kHz in the absence of DNP). The direct ^{31}P spectra recorded at 9.4 T with DNP, and 18.8 T without DNP, are compared in Figure S5. Unfortunately, the intense spinning sidebands resulting from the slower MAS rate preclude the observation of any Q^1 or Q^0 signals in the ^{1}H-^{31}P ramped-CP-MAS spectrum.

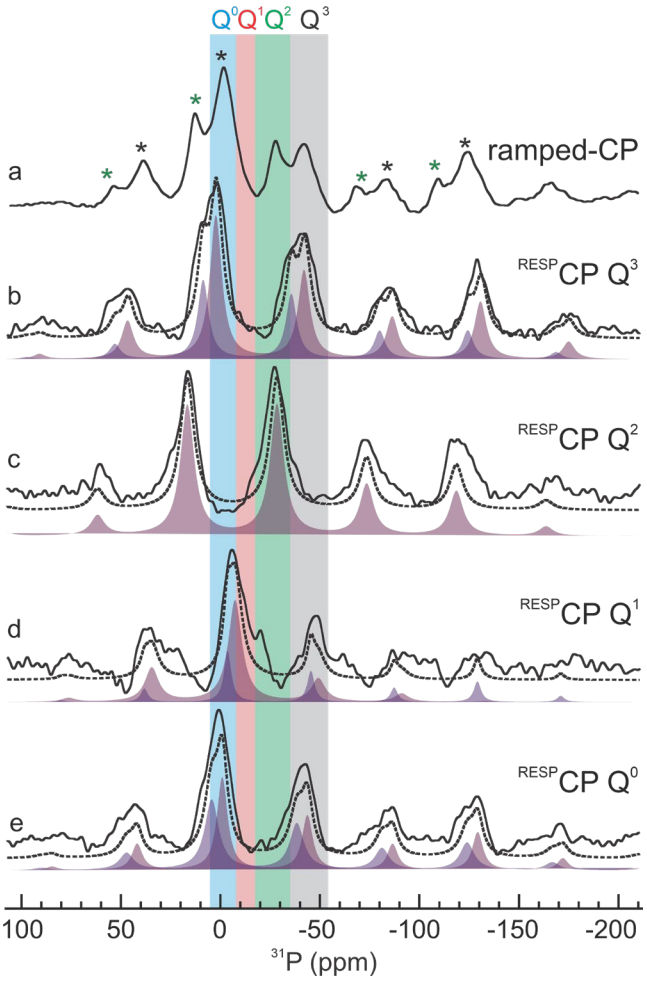

Figure 3. DNP-enhanced ^{1}H-^{31}P CP/MAS spectra (solid black lines) of nearly-dry P-SPP (after 2 min ambient-exposure), recorded using (a) ramped CP, and (b-e) ^{RESPIRATION}CP. In the ^{RESP}CP experiments, the RF frequency was set to (b) -42 ppm, (c) -25 ppm, (d) -11 ppm, or (e) 0 ppm. All spectra were acquired at 9.4 T, 7 kHz MAS, and 95 K. Spinning sidebands for Q^2 and Q^3 signals are indicated by * in green and black, respectively. Simulated spectra (sum: dotted black lines) were obtained with a CSA model, using either a single component (a, c; filled purple spectrum), or two-components (b, d, e; filled spectra in two shades of purple). See Methods section for details. Fit parameters are given in Table 1.

To better resolve the Q^1 and Q^0 signals, we performed frequency-selective CP detection using the ^{RESPIRATION}CP pulse sequence.[60] This approach reveals the distinct sideband pattern of each region. The RF offset frequency was centered sequentially in each of the four Q^n regions ($0 \le n \le 3$). The series of DNP-enhanced ^{RESPIRATION}CP spectra recorded in this way are shown in Figure 3.

Setting the RF offset frequency in the Q^3 region (-42 ppm) enhances the Q^3 signals, while suppressing others. In the ^{RESPIRATION}CP spectrum, the main isotropic peak has a shoulder (Figure 3b), reflecting a second P-site with a chemical shift in this region. The corresponding simulation requires two isotropic signals in the Q^3 region, with chemical shifts C_{iso} of -43 and -36 ppm (Table 1). This result is consistent with the observation of two isotropic Q^3 signals at -43 and -38 ppm by direct ^{31}P MAS NMR at 18.8 T (Figure 2).

Their CSA values of (-147 ± 9) and (-135 ± 30) ppm, respectively), are significantly lower than that reported for P_4O_{10}, -300 ppm.[39] We infer from this comparison that both Q^3 signals arise from P-sites linked to the zeosil framework by P-O-Si linkages. However, unambiguous confirmation of such linkages requires ^{29}Si-^{31}P correlation experiments (see below).

Table 1. CSA parameters for nearly-dry P-SPP, obtained by fitting a simulated spectrum to its ^{RESPIRATION}CP data

RF offset [a] ppm	CS_{iso} [b,c] ppm	CSA [c] ppm	η	LB kHz
-42 (Q^3)	-43 ± 1 (Q^3)	-147 ± 9	0.1	1.2
	-36 ± 2 (Q^3)	-135 ± 30	0.1	1.1
-25 (Q^2)	-28 ± 1 (Q^2)	-127 ± 9	0.1	1.3
-11 (Q^1)	-8 ± 1 (Q^1)	-78 ± 14	0.0	1.4
	-46 ± 2 (Q^3)	-140 ± 45	0.1	0.7
0 (Q^0)	-44 ± 1 (Q^3)	-149 ± 16	0.1	0.9
	-39 ± 1 (Q^3)	-142 ± 15	0.1	1.1

[a] Spectra were recorded at 9.4 T with 7 kHz MAS, using a radiofrequency (RF) offset frequency (in ppm) corresponding in turn to each Q^n region (shown in parentheses). [b] Isotropic chemical shift (in ppm) derived from simulation of the experimental NMR spectrum. The corresponding Q^n region is shown in parentheses. [c] The CS_{iso} and CSA uncertainties represent the variation in each parameter that causes a 1 % decrease in fit quality, defined as the overlap between the simulated and experimental spectra (see Methods section for details).

To observe signals in the Q^2 region, a second ^{RESPIRATION}CP spectrum was recorded with the RF offset frequency set at -25 ppm. The resulting spectrum contains a single isotropic signal with C_{iso} of (-28 ± 1) ppm, Figure 3c, and a CSA of (-127 ± 9) ppm (Table 1). A third ^{RESPIRATION}CP spectrum was recorded with an RF offset frequency set at -11 ppm, in the Q^1 region. The spectrum in Figure 3d contains two peaks within 2 kHz of the RF frequency (i.e., both in the ^{RESPIRATION}CP range). According to the simulated spectrum, the major peak is a spinning sideband of the Q^3 signal at (-46 ± 2) ppm, while the minor peak is an isotropic Q^1 signal at (-8 ± 1) ppm with a relatively small CSA, (-78 ± 14) ppm. For comparison, the isotropic Q^1 signals are completely obscured by spinning sidebands in the ramped-CP spectrum (Figure 3a). Finally, setting the RF frequency to 0 ppm revealed no new isotropic signals, Figure 3e. In this region, Q^0 signals overlap directly with Q^3 spinning sidebands. The spectrum is well-simulated using only CSA parameters for the Q^3 signals (Table 1). All four ^{RESPIRATION}CP experiments were repeated at a different MAS frequency (5 kHz) to confirm the positions of the isotropic peaks (Figure S7).

Overall, the frequency-selective ^{RESPIRATION}CP spectra show that nearly-dry P-SPP contains predominantly P-sites with chemical shifts in the Q^3 and Q^2 regions, with a minor contribution from P-sites with chemical shifts in the Q^1 region. There is no evidence for a significant Q^0 signal in the nearly-dry state. Furthermore, although there are at least two distinct types of P-sites with chemical shifts in the Q^3 region, the observed CSA values suggest that neither corresponds to P_4O_{10}. To be sure that they are covalently bound to the zeosil, the existence of P-O-Si connectivity must be established by direct experiments.

Introducing a more precise nomenclature for P-speciation. The appearance of multiple types of sites with signals in the same Q^n category suggests the need for a more descriptive notation. Here we introduce a more precise nomenclature for P-species using the label Q^n_m, where the upper index (n) represents the total number of P-O-Y bonds. Y can either be Si or P (note that this definition differs from the original definition of n used in Scheme 1). The lower index (m) indicates the number of P-O-Si bonds. Thus, the signal for the surface-bound site $(SiO)_3P{=}O$ is denoted Q^3_3. This notation enables us to distinguish between signals for exclusively surface-bound P-sites ($m = n$), free (poly)phosphoric acid oligomers ($m = 0$) and surface-bound polyphosphoric acid species ($0 < m < n$). It is especially useful for describing "mixed" sites in which a surface-bound P-site is also part of a polyphosphoric acid oligomer. For example, Q^3_2 precisely identifies the Q^3 signal corresponding to the surface-bound P-site (underlined) in $(SiO)_2\underline{P}(O)OP(O)(OX)_2$, where X denotes H or Y (Si or P). Moreover, this notation is readily adapted to describe multinuclear sites. For example, a dinuclear site with two P-sites connected via a P-O-P linkage could be represented by Q^3_2-Q^3_2. Similarly,

Scheme 3. Some of the P-sites possible in P-SPP, including surface-bound sites, free polyphosphoric acid oligomers, and mixed sites.[a] The sites (indicated with colored circles) are grouped horizontally according to chemical shift, and ranked vertically in order of their mobility.

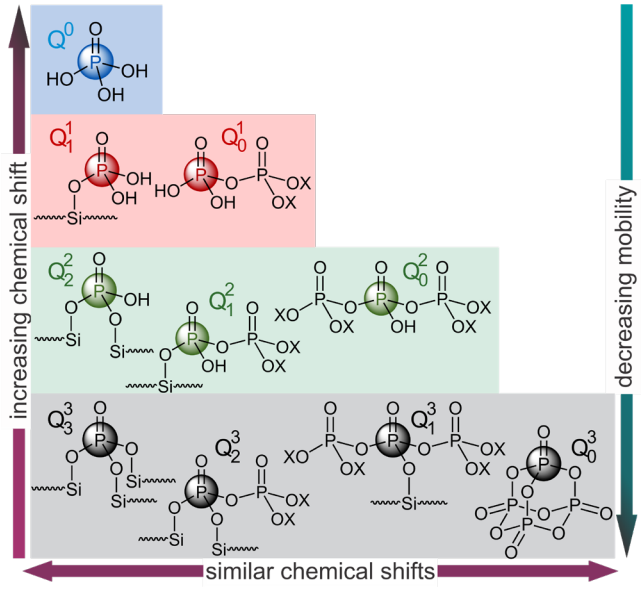

[a] X denotes H, Si or P.

a trinuclear site could be denoted Q^3_2-Q^2_0-Q^3_2. The Q^n_m notation identifies signals with different n values that have distinct chemical shifts, regardless of m. A corollary is that Q^n_m signals with different m values have similar chemical shifts if they have the same n. Therefore, the simpler Q^n designation includes all signals for distinct P-sites with $m \le n$, i.e., with the same number of P-O-H bonds. Q^0_0 is, of course, synonymous with Q^0, because only $m = 0$ is possible. Some of the possible structures for P-sites belonging to the same Q^n categories are shown in Scheme 3.

Impact of hydrolysis on Brønsted acidity in P-SPP. Before attempting to identify P-sites spectroscopically, we explored local P-site structure variations and their potential impact on the Brønsted acidity of P-SPP. Experimental investigations of acidity differences via titration and/or probe reactions are convoluted with changes in site distribution, therefore we undertook an assessment of the relative acidities of a subset of individual P-sites using gas phase electronic structure calculations instead. Due to the complexity of the SPP structure (Scheme 2), we constructed simple cluster models of mono-, di- and trinuclear sites capped with silyl groups (-SiH_3). For example the mononuclear P-sites in P-SPP are represented by Q_3^3, Q_2^2, Q_1^1 and Q^0 cluster models, i.e., the series corresponding to progressive hydrolysis of a Q_3^3 cluster model, according to Scheme 3.

In general, even proton transfers involve the nuclear motion of several atoms. We simplified the problem by limiting our preliminary analysis to a comparison of electronic structures, using a frontier orbital approach. In Mulliken's charge transfer theory, proton transfer starts with formation of a hydrogen-bond between a Brønsted acid (H-bond donor, D) and a base (H-bond acceptor, A), in an acid-base adduct [DH···A].[61–64] In the process, electron density is transferred from a non-bonding pair on the base to an antibonding orbital on the acid. The wavefunction of the acid-base adduct is a superposition of several contributions, including ionic ($D^-\cdots HA^+$) and polar ($D^-\cdots H^+\cdots A$) resonance forms.[65–69] The polar resonance structure is particularly important when the transferring H-in-flight is stabilized electrostatically by the donor and acceptor, especially when there is no activation barrier for proton transfer.[70,71] The D-H heterolytic bond strength (i.e., the deprotonation energy) is therefore a potential descriptor of acidity. However, Keeffe *et al.*[72] demonstrated that these bond strengths correlate poorly when the reaction has an activation barrier. In such cases, *ab initio* calculations confirm the importance of the ionic form to charge transfer between the H-bond donor and acceptor, and the constancy of partial charge on the H-in-flight (0.3-0.5 *e*, depending on the charge localization method).[61,63–65]

For the series of P-acids represented by cluster models here, each interacting with the same base, the relevant antibonding orbital is the lowest unoccupied molecular orbital (LUMO), shown in Figures S14-S17 and the geometric coordinates are given in Table S2. Its energy determines the HOMO-LUMO gap, where a smaller gap corresponds to a more acidic proton. A corollary is that the LUMO energies reflect the relative abilities of each acid site to accept electron density, and relinquish a proton, even without explicit reference to a specific base. For sites with more than one acidic proton, the LUMO of the geometry-optimized structure is delocalized over all chemically equivalent OH groups.

The LUMO energies are given in Figure 4 and Table S3. Of the mononuclear P-site models, the Q_2^2 model is the least acidic, while the Q_1^1 and Q^0 models have similar acidities. Initial hydrolysis of a P-O-Si linkage therefore results in increased acidity. We note that when the P-sites are embedded in the zeosil, some of their POH groups may engage in H-bonding with silanol groups of nearby defect sites. Such interactions will alter the shape of the LUMO and its relative energy, resulting in increased acidity of the remaining (i.e., non-H-bonded) POH groups. For example, a Q_1^1 site might become less acidic than a Q_2^2 site, if one of the OH groups of Q_1^1 is H-bonded.

The impact of H-bonding on acidity is clearly evident in the dinuclear P-site models Q_m^n-$Q_{m'}^{n'}$ (all with a single P-O-P linkage), shown in Figure S15. For each optimized geometry, the number of H-bonds in maximized, and the LUMO is delocalized over the protons that do not participate in H-bonds. The regions of LUMO delocalization correspond to areas of more positive electrostatic potential, where a base would bind more strongly. For example, in the dinuclear Q_0^1-Q_0^1 model cluster with four acidic hydroxyl groups, the minimum energy structure has two hydroxyls H-bonded to O=P groups and two that are free from H-bonding (one on each of the two P-sites). The minimum energy structures for the Q_1^2-Q_0^1 and Q_2^3-Q_0^1 models each have a single non-H-bonded OH, located on the Q_0^1 P-site. In the Q_1^2-Q_1^2 and Q_2^3-Q_1^2 models, all OH groups are engaged in H-bonds in the lowest energy structures.

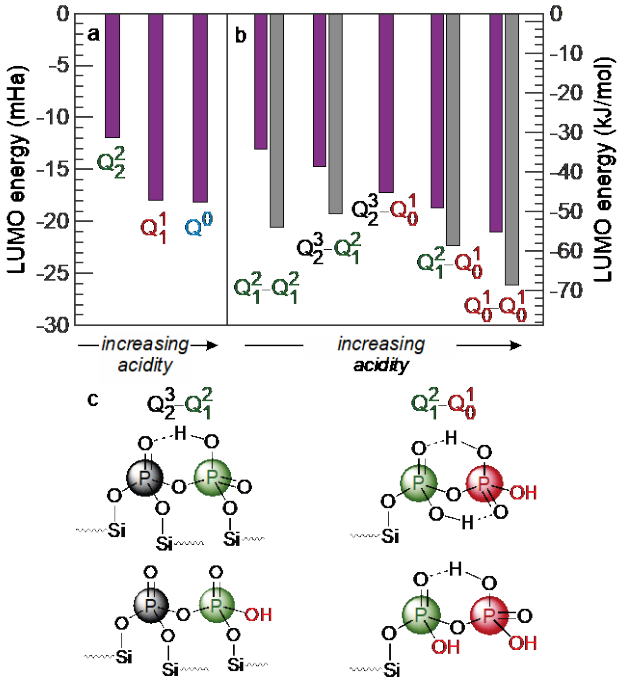

Figure 4. Comparison of calculated energies for the lowest unoccupied molecular orbital (LUMO) in model clusters, for representative P-sites which are (a) mononuclear, and (b) dinuclear. Purple bars represent energies for minimum-energy geometries; gray bars represent higher energy structures with fewer H-bonds. (c) Comparison of structures depict geometries with different numbers of H-bonds, for two of the dinuclear models.

Similar to the mononuclear models, the overall pattern that emerges for many of the dinuclear models is enhanced acidity as the P-O-Si linkages are progressively hydrolysed, in the order Q_2^3-Q_1^2 < Q_2^3-Q_0^1 < Q_1^2-Q_0^1 < Q_0^1-Q_0^1, (Figure 4b and Scheme S1). The predicted acidity of the Q_1^2-Q_1^2 model is anomalously low, likely because it has no hydroxyl groups free of H-bonding in the minimum-energy geometry. The prediction for the Q_2^3-Q_0^1 model may be affected by partly delocalization of its LUMO over a silyl H atom, increasing the acidity of its free OH.

We investigated the impact of H-bonding on acidity in the dinuclear models. Conformations close to the global minimum-energy geometry, but with fewer intramolecular H-bonds, are shown in the gray bars in Figure 4b; some structures are compared in Figure 4c. For example, the Q_0^1-Q_0^1 conformer with one H-bond has a higher total energy (by 11.5 kJ/mol), and a lower LUMO energy (indicating stronger acidity), compared to the global minimum structure with two H-bonds. Disrupting one H-bond in each of the Q_1^2-Q_0^1 and Q_2^3-Q_1^2 models likewise increases the conformer energies, while lowering the corresponding LUMO energies, hence increasing their acidity. We note that the predicted differences in acidity caused by such changes in conformation are similar in magnitude to differences between minimum energy conformers for the dinuclear structures. For example, the higher energy Q_1^2-Q_0^1 conformer is noticeably more acidic than the minimum-energy Q_2^3-Q_0^1 conformer (for the latter, no higher energy structure without the H-bond was located).

The higher energy dinuclear conformers (computed as gas phase models) all appear to be readily accessible at finite temperatures. For example, at ca. 100 °C, they lie within 3 k_BT of their minimum-energy geometries (k_B is Boltzmann's constant). Although H-bonding with silanol groups or framework oxygen atoms is possible in the zeolite, causing the minimum-energy geometries of the P-sites to differ from its gas phase geometry, the situation is expected to be similar (with the caveats that confinement may restrict conformational changes, or modulate the time scales over which they occur). The acidity of an individual P-site is, therefore, dynamic, and a more complete assessment require a statistical model to predict the average acidity for a distribution of species and conformations.

A comparison of the dinuclear and mononuclear model energies in Figure 4 further reveals that P-O-P hydrolysis generally results in *reduced* acidity. For example, the OH group of the Q_0^1 side of the Q_1^2-Q_0^1 site is slightly more acidic than Q^0 itself. Similarly, breaking the P-O-P bond in dinuclear Q_0^1-Q_0^1 yields two mononuclear Q^0 sites that are less acidic than the dinuclear site as reported experimentally[73]. Similar trends are seen in the LUMO energies of trinuclear model sites: the acidity of Q_2^3-Q_0^2-Q_0^1 is higher than that of dinuclear Q_2^3-Q_0^1, formed by P-O-P hydrolysis (Table S3).

Thus, our calculations predict that the presence of water will change P-site acidity in complex ways. In general, we expect an initial increase due to faster hydrolysis of the P-O-Si linkages, followed by a decrease due to slower hydrolysis of the P-O-P linkages. More sophisticated models capable of predicting the evolution of acidity will require a more precise identification of the P-sites present in the P-zeosil as a function of environmental conditions. As a first step towards such insight, we applied 2D MAS NMR techniques to establish P-O-Si and P-O-P connectivity by resolving Q_m^n signals corresponding to structures with different *m* values.

Spectroscopic evidence for surface-bound P-sites. P-O-Si linkages have been identified in well-defined, crystalline silicophosphates, via their ^{29}Si and ^{31}P NMR spectroscopic signatures.[32,41,74] For example, the ^{29}Si signal at ca. -210 ppm for six-coordinate Si atoms in crystalline $Si_5O(PO_4)_6$ was associated with a ^{31}P signal at -44 ppm using *J*- and *D*- based 2D correlation spectroscopy.[32] Mixed-phase materials such as silicophosphate gels, consisting of the crystalline phases $Si_5O(PO_4)_6$, $Si(HPO_4)_2{\bullet}H_2O$ and SiP_2O_7 as well as amorphous phases, have also been studied by ^{29}Si and ^{31}P NMR.[30,31,40] While P-O-Si linkages were identified in the crystalline phases, peak assignments for the amorphous phase were ambiguous due to chemical shift overlap for species with P-O-P and/or P-O-Si linkages (Scheme 1).

Since we ruled out P_4O_{10} as the origin of Q^3 signals based on comparison of their CSA values, the signals must arise from sites that contain P-O-Si linkages. Candidates include Q_3^3 and $Q_2^3 - Q_2^3$ sites. With DNP-induced signal amplification, it becomes feasible to establish the presence of P-O-Si linkages based on through-space dipolar coupling between ^{29}Si and ^{31}P. Specifically, a Double CP (DCP) pulse sequence[75] can selectively detect ^{31}P NMR signals from sites that are spatially proximal to ^{29}Si. Since the DCP transfer efficiency depends on through-space dipolar coupling from ^{1}H to ^{29}Si to ^{31}P, only ^{31}P sites connected to nearby ^{29}Si sites (e.g., surface-bound P-sites) yield strong intensities, while P-sites that interact weakly with ^{29}Si atoms in the zeosil framework should result in low or no intensity.

DNP-enhanced ^{31}P MAS-NMR spectra recorded for nearly-dry P-SPP, with and without ^{29}Si-filtering, are compared in Figure 5a. The strong signal intensities observed for both the Q^3 and Q^2 regions of the ^{29}Si-filtered DCP spectrum suggest that these include P-sites with P-O-Si linkages. Due to the low overall DCP efficiency, the evidence is only qualitative. Even so, the total intensity of the Q^3 signals (including their spinning sidebands) relative to the Q^2 signals is higher in the ^{29}Si-filtered ^{31}P DCP spectrum compared to the ramped ^{1}H-^{31}P CP spectrum. This finding implies that P-sites with signals in the Q^3 region have, on average, more P-O-Si linkages than P-sites with signals in the Q^2 region. The minor Q^1 signal observed via $^{\text{RESPIRATION}}$CP is not resolved in the CP and DCP spectra, and hence will not be discussed further here.

More quantitative information about the average ^{29}Si-^{31}P coupling strength was sought for each group of P-sites by acquiring buildup curves. Figure 5c shows how the peak intensity for each type of Q^n signal in the ^{29}Si-filtered ^{31}P DCP spectra (I_{DCP}) varies relative to its intensity in the ^{31}P CP spectrum (I_{CP}), as a function of the DCP mixing time, τ_{DCP}. A mono-exponential equation, $I_{DCP}/I_{CP} = a(1\text{-}\exp(-\tau_{DCP}/T_{DCP}))$, was refined to the data to obtain the buildup time constant T_{DCP}. I_{DCP}/I_{CP} is the ratio of the peak intensities in the DCP and CP spectra for a given value of τ_{DCP}, and the constant *a* is the asymptotic value of the corresponding ratio. In the absence of nuclear spin relaxation, the latter corresponds to the fraction of ^{31}P sites with at least one P-O-Si linkage, assuming 100 % DCP efficiency. (Since in practice the DCP efficiency is lower, the value of *a* is difficult to interpret quantitatively, therefore we will not discuss the refined values further.)

For nearly-dry P-SPP, the value of T_{DCP} for the Q^3 signals is (20.0 ± 0.9) s. This is shorter than for the Q^2 signals, (32.8 ± 7.1) s, indicating that the P-sites responsible for the Q^3 signals are more strongly coupled to Si relative to those responsible for the Q^2 signals. This finding is consistent with the relative intensities of the signals in the ^{29}Si-filtered ^{31}P DCP spectra (Figure 5a).

Thus nearly-dry P-SPP contains at least two major P-sites with signals in the Q^3 region (differing in chemical shifts and CSAs), neither of which is P_4O_{10}, and at least one major site with a signal in the

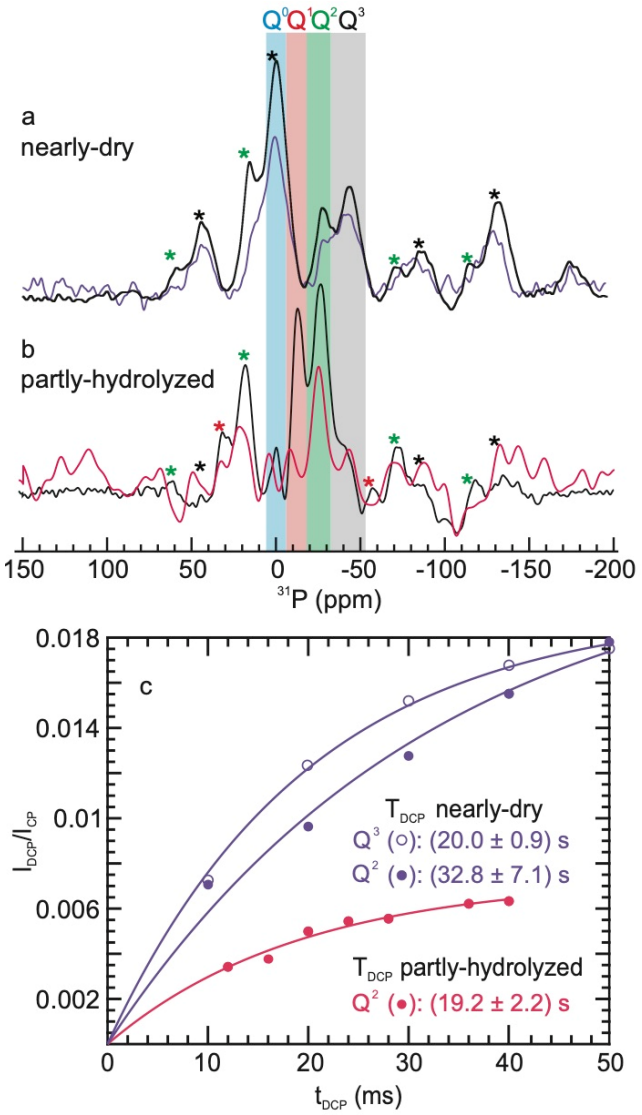

Figure 5. Comparison of DNP-enhanced ^{1}H-^{31}P CP and ^{29}Si-filtered ^{31}P DCP MAS-NMR spectra (a,b), and the corresponding DCP buildup curves (c), for nearly-dry and partly-hydrolyzed P-SPP. Both ^{1}H-^{31}P CP spectra (black) were acquired in 16 scans. The DCP spectra (colored) were acquired for (a) nearly-dry material (2048 scans), and (b) partly-hydrolyzed material (768 scans), prepared by exposure of the dry material to air for 2 or 10 min, respectively. Both were recorded with a 40 ms mixing time (τ_{DCP}). Spinning sidebands for Q^1, Q^2, and Q^3 signals are indicated by * in red, green, and black, respectively. (c) ^{31}P DCP peak intensity relative to CP intensity (both normalized by number of scans), for various signals as a function of mixing time. The solid lines are curvefits obtained using a mono-exponential model (see below). Experimental spectra for all mixing times, and the regions used to obtain the peak areas, are shown in Figure S8.

Q^2 region. P-sites with signals in the Q^1 region make a minor contribution. P-O-Si linkages are present in all major sites, but are relatively more abundant in those with Q^3 signals. Table 2 shows the minimum number of structures required to account for the experimental observations for dry/nearly-dry P-SPP. The slower buildup of the Q^2 signals is consistent with Q^3_2-Q^2_1 sites formed by hydrolysis of Q^3_2-Q^3_2, or with non-surface-bound Q^2_0 sites, possibly as part of more complex, trinuclear P-sites such as Q^3_2-Q^2_0-Q^3_2.

To probe the sensitivity of the P-O-Si linkages to water, P-SPP was partly-hydrolyzed by increasing the ambient exposure time to 10 min. In the ^{1}H-^{31}P CP spectrum (without ^{29}Si-filtering), the signal intensity in the Q^3 region of the partly-hydrolyzed material is much lower (Figure 5b) relative to that of the nearly-dry material (dominated by Q^3 signals). The signal intensities in both the Q^2 and Q^1 regions are comparable, and higher than in the Q^3 region. Furthermore, a small Q^0 signal representing H_3PO_4 that was absent in the spectrum of the nearly-dry material becomes visible for the partly-hydrolyzed material. For all τ_{DCP} values tested, the residual Q^3 signal is weak in the ^{29}Si-filtered DCP spectrum of the partly-hydrolyzed material, Figure S8b. Given the low peak intensity, the T_{DNP} value could not be measured. Nevertheless, the persistence of a Q^3 signal suggests that some surface-bound Q^3 P-sites (e.g., Q^3_3 and/or Q^3_2) remain.

Table 2. Spectroscopic evidence for proposed structures of major mononuclear and dinuclear P-sites present in P-SPP, in three different hydration states

Label	Structure	Hydration state		
		Nearly dry	Partly hydrolyzed	Fully hydrolyzed
Q^3_3	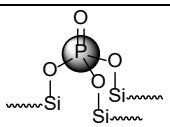	DCP		
Q^3_2-Q^3_2	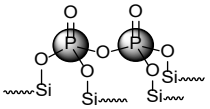	DCP	DCP	
Q^2_1-Q^2_1	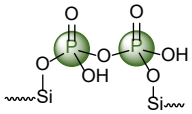	DCP	DCP	
Q^2_2	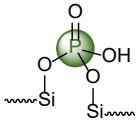		DCP	
Q^1_0-Q^1_0	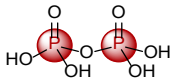		DCP	DCP
Q^0	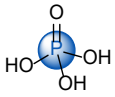			DCP
Q^3_2-Q^2_1		RFDR	RFDR	
Q^2_1-Q^1_0	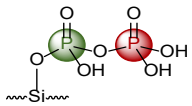		RFDR	

The most intense signal, in the Q^2 region, arises from surface-bound P-sites with lower CSA relative to the nearly-dry state (i.e.,

Q_2^2 and/or Q_1^2). Moreover, the buildup time for this signal, (19.2 ± 2.2 s), is much shorter than for the nearly-dry material (32.8 ± 7.1 s), suggesting that partial hydrolysis leads to a new type of surface-bound P-site in the Q^2 region. The most likely candidate is Q_2^2, arising from hydrolysis of Q_3^3 (Scheme 4 and Scheme S2). Finally, the suppression of the Q^1 signal in the ^{29}Si-filtered ^{31}P DCP spectrum is consistent with its assignment to Q_0^1, arising from P-sites that are not surface-bound. The poor SNR for signal in the Q^1 region precludes measurement of an accurate buildup time for this signal. Table 2 shows the minimum number of structures required to account for the spectra of the P-sites in partly-hydrolyzed P-SPP.

The CP and DCP experiments were repeated after exposure of P-SPP to air for 10 d to generate a fully-hydrolyzed material (Figure S8c). Both NMR spectra are dominated by the signal corresponding to H_3PO_4 (Q^0), which remains associated with the zeolite but lacks P-O-Si linkages. The overall SNR of the ^{29}Si-filtered ^{31}P DCP spectrum is significantly lower compared to spectra of the nearly-dry or partly-hydrolyzed material, consistent with cleavage of all P-O-Si linkages. As expected, the DCP buildup time for the Q^0 peak in the fully-hydrolyzed material is very slow, (50 ± 11) s (Figure S9), compared to the Q^3 and Q^2 buildup rates in the nearly-dry and partly-hydrolyzed states.

These DCP experiments provide direct evidence for P-O-Si linkages in dry P-SPP, and their hydrolysis with increasing exposure to water. However, a coherent explanation for the spectroscopic observations requires P-species containing P-O-P as well as P-O-Si linkages. The minimum number of structures required therefore includes the dinuclear P-sites shown in Table 2. To verify this hypothesis, we investigated the presence of P-O-P′ linkages in P-SPP using 2D ^{31}P-^{31}P correlation spectroscopy. The results allow us to assess the relationships between sites containing P-O-P linkages and those with P-O-Si linkages, and to evaluate their relative hydrolytic stabilities.

Spectroscopic evidence for P-O-P′ linkages. The existence of oligomers in concentrated phosphoric acid solutions is well-known.[4] To investigate the presence of oligomers containing P-O-P linkages in P-SPP, we acquired homonuclear ^{31}P-^{31}P correlation spectra, using a radio-frequency-driven recoupling (RFDR) pulse sequence.[76] Polarization is transferred from one P-site to a nearby P-site via dipolar (through-space) coupling. For P-sites directly linked via a bridging oxygen (P-O-P), the coupling was reported to be ca. 900 Hz (described as "strongly-correlated").[39] Numerical simulations based on quantum mechanics suggest that an RFDR mixing time (τ_{RFDR}) of ca. 700 μs is optimal to detect strongly-correlated P-sites (Figure S10). Adjacent P-sites not connected by P-O-P linkages, i.e., "weakly-correlated" sites with dipolar couplings <900 Hz, require a longer τ_{RFDR} for efficient polarization transfer.

Figure 6a shows the 2D homonuclear ^{31}P-^{31}P correlation spectrum for nearly-dry P-SPP, recorded with DNP enhancement. It includes isotropic self-correlations (along the main diagonal) and correlations between each isotropic signal and its sidebands (along the secondary diagonals, parallel to the main diagonal but separated from it by the spinning frequency). The main on-diagonal peaks at (-29, -29), (-43, -43) ppm are self-correlations of the Q^2 and Q^3 signals, respectively; the self-correlation of a Q^3 spinning sideband is visible at (-1, -1) ppm. Peaks on the secondary diagonals at (-1, -43) and (-43, -1) ppm are self-correlations between the isotropic Q^3 signals and their spinning sidebands.

The key new information in these data is contained in the off-diagonal peaks, or cross-peaks, which indicate proximity between P-sites with different chemical shifts. They reveal proximal P-sites

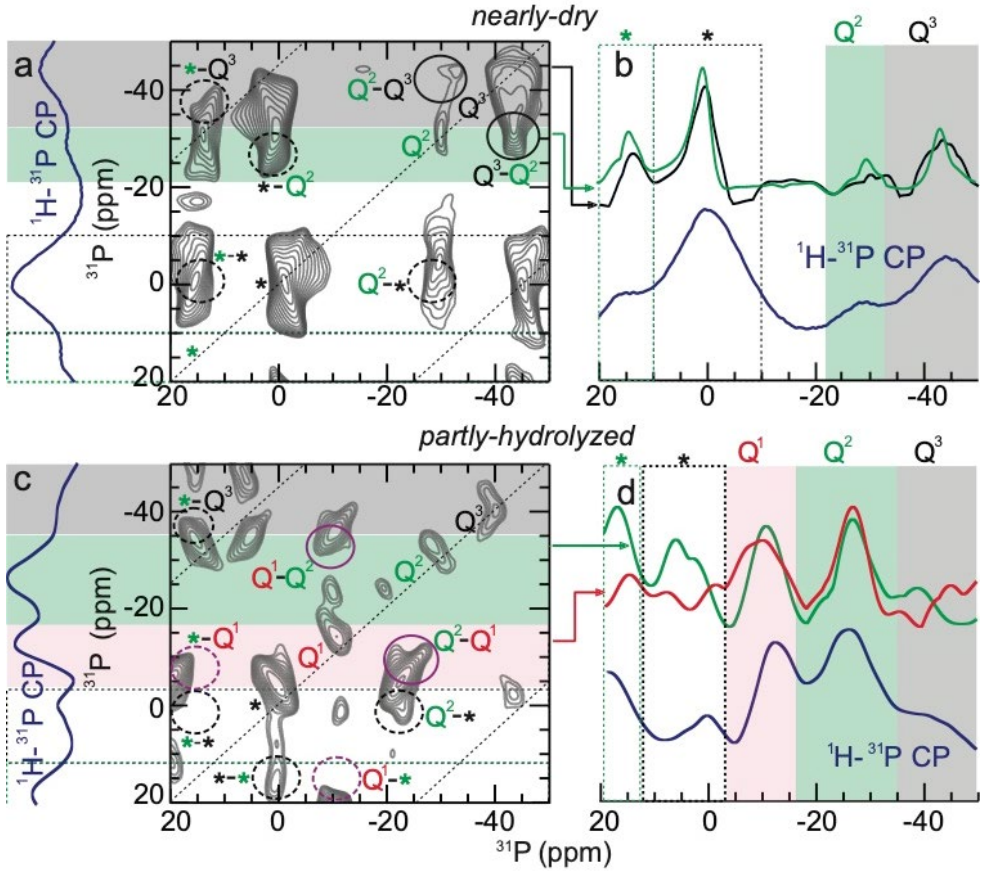

Figure 6. DNP-enhanced ^{31}P-^{31}P correlation spectra and their 1D projections for: (a,b) nearly-dry P-SPP, and (c,d) partly-hydrolyzed P-SPP. Both spectra were recorded at 9.4 T and 7 kHz MAS, with an RFDR mixing time of 714 μs. For reference, the corresponding ^{1}H-^{31}P CP spectra are shown to the left of the 2D plots, and below the 1D projections in blue. The gray, green and red shaded stripes highlight the Q^3, Q^2, and Q^1 regions, respectively. The corresponding sideband regions are shown by the dashed (unshaded) stripes (same color codes). Asterisks denote spinning sidebands for Q^3 (gray) and Q^2 (green) signals, respectively. Solid circles denote Q^3-Q^2 (black) and Q^2-Q^1 (purple) cross-peaks, respectively. Dashed circles indicate cross-peaks involving a spinning sideband.

whose Q^n signals correspond to different *n* values (i.e., P-O-P′ linkages). Off-diagonal cross-peaks are located at (0, -30), (-30, 0), (-30, -43) and (-43, -30) ppm. Their chemical shift values indicate a correlation between a Q^3 signal (or its spinning sideband) and a Q^2 signal. These cross-correlations can also be observed in the 1D projections of the regions for different Q^n signals. Figure 6b compares these projections for the Q^3 and Q^2 regions with the ^{1}H-^{31}P CP spectrum (blue). The row from the Q^3 region (black) clearly contains the Q^2 signal, while the row from the Q^2 region (green) also clearly contains the Q^3 signal. This result confirms a strong correlation between Q^3 and Q^2 signals, arising from dinuclear P-sites.

Even if present, proximal P-sites whose Q^n signals correspond to the same *n* and *m* values (i.e., identical P-sites linked by P-O-P, such as Q^3_2-Q^3_2), cannot be distinguished from self-correlations in the 2D RFDR spectra. Although cross-peaks for signals with the same *n* value but different *m* values, such as Q^3_2-Q^3_1, are in principle observable, they will appear near the broad on-diagonal peaks and may be difficult to resolve. Double quantum-single quantum (DQ-SQ) NMR experiments[77] could be used to obtain correlations between such sites with similar chemical shifts. However, our attempts to conduct such experiments with P-SPP using the supercycled POST C5 (SPC5) pulse sequence[78] were unsuccessful, most likely due to the large ^{31}P CSA and/or rapid ^{31}P relaxation.

To confirm that the cross-peaks in the RFDR spectra of the nearly-dry material arise due to intramolecular P-O-P′ linkages, rather than intermolecular correlations, the same 2D experiment was repeated with a longer mixing time (Figure S11). The optimum mixing time for weakly-coupled P-sites (i.e., those not linked via P-O-P′) should be significantly longer. However, the intensities of the cross-peaks relative to the diagonal peaks did not increase upon doubling τ_{RFDR} from 714 to 1428 μs (see Figures S11-S13). Thus, the Q^3-Q^2 cross-peaks arise from strongly-correlated (P-O-P′-linked) dinuclear sites. This observation is consistent with the presence of Q^3_2-Q^2_1 sites, as shown in Table 2. Their presence in nearly-dry P-SPP was suggested by the $^{\text{RESPIRATION}}$CP results (Figure 3b), which revealed a second type of Q^3 site (in addition to mononuclear Q^3_3). The postulated Q^3_2-Q^3_2 sites should generate Q^3_2-Q^2_1 sites upon hydrolysis. Such a transformation is consistent with the greater susceptibility of the P-O-Si linkage relative to the P-O-P linkage.

The RFDR spectrum of partly-hydrolyzed P-SPP shows on-diagonal peaks for all four Q^n regions (Figure 6c). A pair of cross-peaks at (-12, -26) and (-26, -12) ppm correlates Q^1 and Q^2 signals, and hence implies a P-O-P′ relationship between them. A second pair of

cross-peaks at (-2, +18) and (+18, -2) ppm correlates Q^3 and Q^2 spinning sidebands. A cross-peak at (-23, -2) ppm relates the

Scheme 4. Proposed structures for the major P-sites in P-SPP and their corresponding Q^n_m signal designations, as well as their likely hydrolysis pathways.

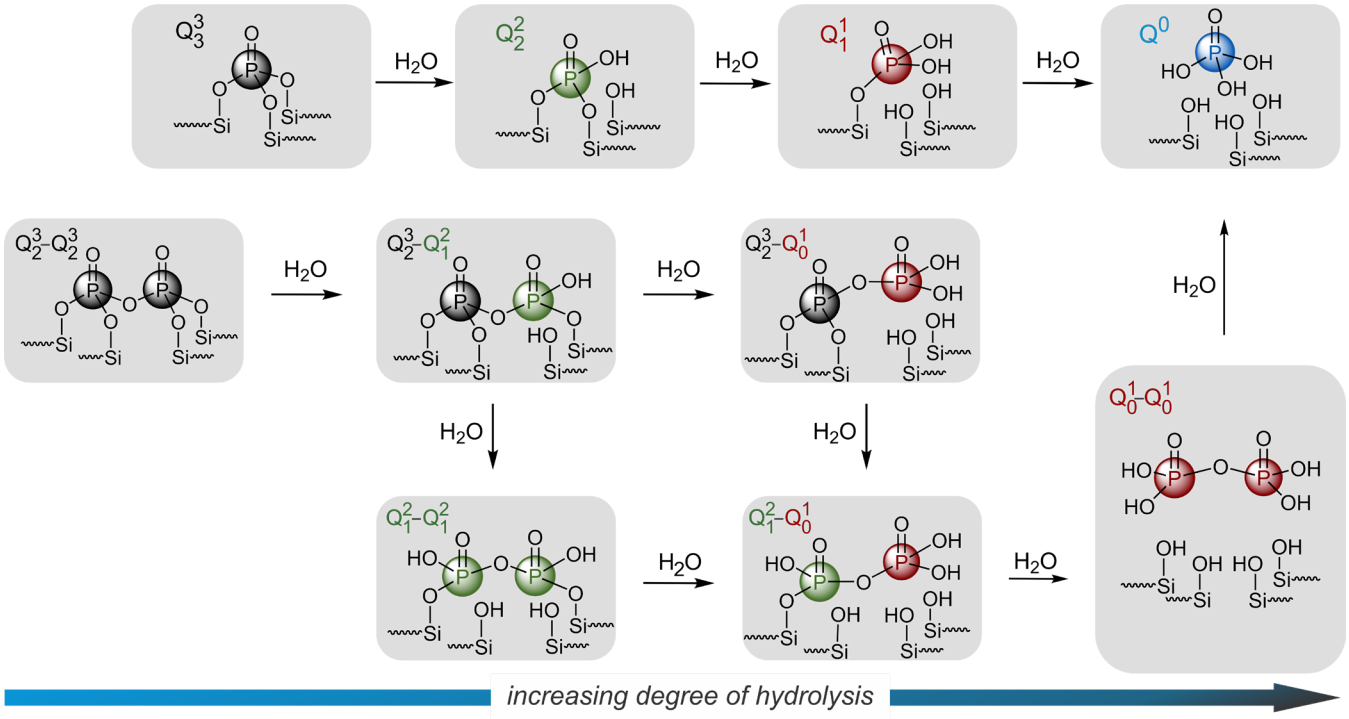

isotropic Q^2 signal to a Q^3 spinning sideband, while a cross-peak at (+15, -38 ppm) relates a Q^2 sideband to the isotropic Q^3 signal. These correlations confirm the existence of P-O-P′ linkages in two kinds of dinuclear P-sites, giving rise to Q^2-Q^1 and Q^3-Q^2 signals (Table 2). The 1D projections of the corresponding rows in the Q^2 (green) and Q^1 (red) regions show the appropriate cross-peaks (Figure 6d). In combination with the ^{29}Si-filtered ^{31}P DCP NMR results, this finding suggests two kinds of dinuclear P-sites in partly-hydrolyzed P-SPP, depicted in Table 2 as Q^3_2-Q^2_1 and Q^2_1-Q^1_0.

Origin of the P-site distribution in P-SPP. Based on all the spectroscopic information presented thus far, the P-sites and their hydrolysis pathways are summarized in Scheme 4. Due to the low P-loading (Si/P = 27), we consider only mononuclear and dinuclear P-sites in this minimal model. However, the co-existence of larger oligomers in P-SPP cannot be ruled out. Certain trinuclear mixed species, shown in the SI, would also give signals consistent with the experimental observations.

In the top row of Scheme 4, surface-bound Q^3_3 sites reflect condensation of H_3PO_4 with silanol nest defects in the SPP micropores and/or external (mesopore) silanols. These sites should be converted by hydrolysis to Q^2_2, Q^1_1, and finally, Q^0 sites. Both Q^3_3 and Q^2_2 signals are present in the spectrum of the partly-hydrolyzed material. However, the NMR signature of surface-bound Q^1_1 was not observed in the ^{29}Si-filtered ^{31}P DCP spectrum of partly-hydrolyzed P-SPP, suggesting that this site is particularly unstable towards hydrolysis, and hence evades detection.

In the second row of Scheme 4, dinuclear surface-bound Q^3_2-Q^3_2 sites reflect reactions of $H_4P_2O_7$ with silanol nests. Hydrolysis of one of the P-O-Si bonds would result in formation of Q^3_2-Q^2_1 sites (consistent with the DCP results reported above, and confirmed by RFDR). Further P-O-Si hydrolysis would account for our observations of several mixed P-sites: Q^3_2-Q^1_0, Q^2_1-Q^2_1, and Q^2_1-Q^1_0 as well as free pyrophosphoric acid (Q^1_0-Q^1_0). The intermediate hydrolysis products Q^2_1-Q^2_1 and Q^1_0-Q^1_0, while expected, cannot be observed by RFDR. However, the presence of Q^1_0-Q^1_0 sites can be inferred from the observation of a Q^1 signal in the ^{1}H-^{31}P CP spectrum of partly hydrolyzed P-SPP (Figure 5b), combined with the finding that these are not Q^1_1 sites based on analysis of the ^{29}Si-filtered ^{31}P DCP spectrum. Thus we conclude that the Q^1 signals represent Q^1_0-Q^1_0 sites. Eventually, all surface-bound P-sites are converted to Q^0 sites in the fully-hydrolyzed state. However, the persistence of P-O-P linkages and the late appearance of the Q^0 signal, is consistent with the expected greater hydrolytic instability of P-O-Si relative to P-O-P.

CONCLUSIONS

Phosphorus-modified self-pillared pentasil (P-SPP) is highly selective in the formation of biomass-derived commodity chemicals such as *p*-xylene and butadiene.[14,15] The origin of the catalytic activity lies in the structures of its confined P-sites, whose moderate Brønsted acidity (P-OH) promotes selective transformations aided by the shape- and size-constraints of the zeolite micropores. The nature of the P-sites, including how they interact with the zeolite framework and with each other, was explored using DNP-enhanced solid-state NMR spectroscopy, including $^{\text{RESPIRATION}}$CP NMR, ^{29}Si-filtered ^{31}P DCP NMR, and 2D ^{31}P-^{31}P correlation NMR, in combination with DFT calculations. Dry P-SPP contains predominantly two

types of fully-condensed P-sites: mononuclear (Q^3_3) and oligomeric (most likely dinuclear, Q^3_2-Q^3_2). Although neither is acidic, the NMR results confirm that both are surface-bound. Their presence was confirmed by ^{29}Si-filtered ^{31}P DCP correlation NMR spectroscopy. The mononuclear site undergoes hydrolysis of a P-O-Si linkage to form a Q^2_2 site, before eventually being converted to H_3PO_4 (Q^0), presumably via an unstable Q^1_1 intermediate.

Frequency-selective detection using $^{\text{RESPIRATION}}$CP suggests the presence of additional dinuclear P-sites with *both* P-O-Si and P-O-P linkages in dry P-SPP. The most likely candidate is surface-bound Q^3_2-Q^3_2. It is rapidly converted to a Q^3_2-Q^2_1 site, detected by 2D ^{31}P-^{31}P correlation NMR, via selective hydrolysis of a P-O-Si linkage when the zeolite is briefly exposed to moisture. Further hydrolysis leads to the formation of other surface-bound dinuclear sites such as a Q^2_1-Q^1_0 site, leading eventually to non-surface-bound $H_4P_2O_7$ (Q^1_0-Q^1_0). The P-O-P linkage is the last to hydrolyze, finally forming H_3PO_4 (Q^0).

This study reveals that the Brønsted acidity in P-SPP arises from a diverse mixture of partly-hydrolyzed surface-bound and non-surface-bound mononuclear and dinuclear sites, even at low P-loadings (P/Si = 27). The presence of trinuclear and higher oligomers cannot be excluded, and are presumably even more important for zeosils with higher P contents. The P-site distribution is determined by the extent of hydrolysis, and has important consequences for the Brønsted acidity. Although the precise identities of the active sites in P-zeosils have yet to be established, and must be under reaction conditions, this work represents a step toward the rational design of supported acid catalysts with improved activity and selectivity.

METHODS

Sample preparation. P-modified self-pillared pentasil (P-SPP), with Si/P = 27, was synthesized following a previously described procedure.[19] The material was dried by dehydration at 450 °C and <10^{-4} Torr for 12 h, then packed and sealed in a 3.2-mm zirconia NMR rotor in a N_2-filled glove-box. To obtain partially hydrolyzed materials, the rotor cap was removed manually for a short period of time (timed with a stopwatch), then replaced. Air-exposure times are approximate. The experiments reported in Figure 2 were performed on consecutive days, when the relative humidity varied between 74 and 78 % during the measurement time.

Direct excitation solid-state MAS-NMR spectroscopy. ^{31}P MAS-NMR measurements were performed at room temperature on a Bruker AVANCE III Ultrashield Plus 18.8 T Spectrometer (corresponding to ^{1}H and ^{31}P frequencies of 800 and 323.85 MHz, respectively) at a MAS frequency of 20 kHz. The sample was packed in a 3.2 mm zirconia rotor with N_2 gas as both bearing and drive gas to ensure a no exposure to moisture during data acquisition. A single 90 ° excitation pulse of length 7 μs was used on the ^{31}P channel. An aqueous phosphoric acid solution (1 M) provided the chemical shift reference.

DNP-enhanced MAS-NMR spectroscopy. To acquire DNP-enhanced MAS-NMR spectra, 1,1,2,2-tetrachloroethane (TCE, Sigma-Aldrich) was dried using standard procedures[79] and stored over molecular sieves in a Schlenk flask equipped with a Teflon stopcock. The TEKPOL biradical (Cortecnet) was dissolved in TCE under N_2 atmosphere to give a 16 mM solution. In a N_2-filled glove-box, dehydrated P-SPP (30 mg) was mixed with 60 μL of the biradical solution. The resulting paste was packed into 3.2-mm sapphire rotor and sealed in a glass ampule for transfer to the spectrometer. No radical quenching was observed within one week of rotor packing, as judged by the lack of apparent change in the ^{31}P NMR intensities. Experiments were performed on a Bruker 400 MHz MAS-DNP-NMR system at 9.4 T and -178 °C, using as MAS frequency either 5 or 7 kHz. The latter is the maximum spinning rate we can achieve under DNP conditions. Ramped Cross-polarization (ramped-CP), with a ramp on the ^{1}H channel and a rectangular shape on the X (^{31}P or ^{29}Si) channel, was applied to accomplish both ^{1}H-^{31}P and ^{1}H-^{29}Si polarization transfers. The CP efficiency was optimized by varying the RF amplitude (power level) on the X channel while fixing the proton RF amplitude at 68 kHz, with a ramp from 70 to 100 % power. For ^{1}H-^{31}P CP, a contact time of 2 ms was used, with SPINAL-64 decoupling (RF amplitude 110 kHz and 3.8 μs pulse length) during acquisition. Frequency-selective ^{1}H-^{31}P cross-polarization was achieved using the Rotor Echo Short Pulse Irradiation Cross-Polarization ($^{\text{RESPIRATION}}$CP) pulse sequence,[60] with short pulse length of 5 μs. CSA parameter fitting was performed using the Solid Line Shape Analysis (SOLA) toolbox in Topspin-4.0.6 (Bruker), which uses the Haeberlen convention[80] for the chemical shift tensor parameters, $|\delta_{zz} - \delta_{iso}| \geq |\delta_{xx} - \delta_{iso}| \geq |\delta_{yy} - \delta_{iso}|$, where the isotropic CS is defined as $\delta_{iso} = (\delta_{11} + \delta_{22} + \delta_{33})/3$, the CSA is $\Delta\delta = \delta_{zz} - (\delta_{xx} + \delta_{yy})/2$, and the asymmetric parameter is $\eta = (\delta_{yy} - \delta_{xx})/(\delta_{zz} - \delta_{iso})$. The program uses a simplex algorithm to optimize the overlap between simulated and experimental spectra by varying the chemical shift tensor parameters, and line-broadening in each iteration. The uncertainties in the fit parameters were determined by manually varying the CSA and CS_{iso} one by one from the optimum values until the overlap decreased by ±1 %. This change resulted in a visually detectable decrease in fit quality. Reported parameter values are the average of the values in the two error limits.

^{29}Si-filtered ^{31}P DCP spectra were recorded by exciting the ^{29}Si sites using 10 ms of ^{1}H-^{29}Si CP (Figure S18) contact time, prior to the DCP block for the ^{29}Si-^{31}P polarization transfer. The ^{1}H-^{29}Si mixing time was optimized to maximize ^{29}Si peak intensities. During DCP, the RF amplitude on the ^{29}Si channel was varied adiabatically using a tangential shape,[81] while a square pulse was used on the ^{31}P channel and SPINAL-64 decoupling (110 kHz RF amplitude and 3.8 μs pulse length) on the ^{1}H channel . The RF amplitudes during the DCP block were optimized by varying the power level on the ^{31}P channel while keeping the ^{29}Si power level fixed. The optimum amplitudes were found to be 39.5 and 31.5 kHz on the ^{29}Si and ^{31}P channels, respectively. Previously, the mixing time τ_{DCP} = 40 ms (used for ^{29}Si-^{31}P polarization transfer via DCP) was shown to be optimal for detecting P-O-Si linkages in previous studies of silicophosphates.[74] To record buildup curves of nearly-dry and hydrolyzed materials, τ_{DCP} was varied from 10 to 50 ms in steps of 10 ms. For the partly-hydrolyzed material, τ_{DCP} was varied from 10 to 40 ms in steps of 5 ms. Peak intensities for the nearly-dry material were determined by summing the areas under the isotropic peaks in the region -20 to -65 ppm, as well as the areas under the most intense of the corresponding spinning sidebands, i.e., in the region from +30 to -15 ppm. For the partly-hydrolyzed material, only the isotropic peak intensities were considered because the sidebands are much weaker. To obtain I_{DCP}/I_{CP} and plot the buildup curves, the area under each peak and its corresponding sidebands was normalized by the number of scans, then divided by the normalized ^{1}H-^{31}P CP peak area in the same region. The buildup time T_{DCP} was obtained from each buildup curve using a simple mono-exponential model, $I_{DCP}/I_{CP} = a(1\text{-}\exp(-\tau_{DCP}/T_{DCP}))$.

^{31}P-^{31}P correlation spectra were recorded using a Radio Frequency Driven Recoupling (RFDR) pulse sequence. DNP-enhanced ^{1}H-^{31}P ramped-CP was used with the aforementioned parameters to increase sensitivity. RFDR was performed using 180 ° pulses of length 5.6 μs on the ^{31}P channel for two mixing times: 714 and 1428 μs, corresponding to 5 and 10 rotor periods, respectively, at 7 kHz MAS. 2D experiments were performed using 160 increments in the indirect dimension, with 8 scans per increment. ^{1}H decoupling was achieved with SPINAL-64 decoupling (110 kHz RF amplitude and 3.8 μs pulse length) during the acquisition and the indirect delay, while CW irradiation (110 kHz amplitude) was used during RFDR mixing period. The 1D projections were calculated in Topspin-4.0.6 by summing the rows of the 2D spectrum in the range -49 to -34 ppm for Q^3, -32 to -21 ppm for Q^2 and -6 to 7 ppm for * (spinning sideband of Q^3). The ratio of the areas of the off-diagonal peaks to the diagonal peaks was used to determine the extent of polarization transfer.

The numerical simulations for determining the optimum RFDR mixing time were performed using SIMPSON-4.0.[82] A spin system was constructed with

two ^{31}P spins, corresponding to Q^2 and Q^3 signals with appropriate chemical shift tensor parameters (isotropic chemical shifts of -43 and -29 ppm, and anisotropies of -190 and -125 ppm, respectively). The MAS frequency of 7 kHz and proton frequency of 400 MHz were used in the simulations to mimic the experimental conditions. Buildup curves were simulated for dipolar couplings of 1200, 900, 600, and 300 Hz (Figure S10). For a P-P dipolar coupling typical of a P-O-P linkage (ca. 900 Hz), maximum polarization transfer using RFDR was achieved after ca. 700 μs.

Electronic structure calculations. All electronic structure calculations were performed with Gaussian 09[83] at the M062X/aug-cc-pvtz level of theory. The SCF cycle convergence was set at 10^{-8}, and optimized geometries were converged to 0.0003 Ha/Bohr. Stationary points were verified by vibrational frequency analysis (zero imaginary frequencies).

ASSOCIATED CONTENT

Supporting Information

The Supporting Information is available free of charge on the ACS Publications website.

Additional ^{31}P and ^{29}Si 1D MAS-NMR spectra, 2D RFDR spectra and RFDR buildup curves. Diagrams and coordinates of cluster models showing DFT-optimized geometries. Tables of CSA fit parameters for ^{31}P MAS spectra and LUMO energies of cluster models. (PDF)

AUTHOR INFORMATION

Corresponding Authors

* Songi Han
Department of Chemistry & Biochemistry
Department of Chemical Engineering
University of California Santa Barbara
Santa Barbara, California 93106 United States
songihan@ucsb.edu
* Susannah L. Scott
Department of Chemistry & Biochemistry
Department of Chemical Engineering
University of California Santa Barbara
Santa Barbara, California 93106 United States
sscott@ucsb.edu

Present Address

⊥Zhang Dayu School of Chemistry, Dalian University of Technology, No. 2 Linggong Road, Dalian, 116024, China

Author Contributions

‡S.K.J. and T.T. contributed equally.

Funding

SKJ conducted the NMR measurements, SC performed the DFT calculations, and LR synthesized the materials, all with support from the Catalysis Center for Energy Innovation, an Energy Frontier Research Center funded by the U.S. Department of Energy, Office of Science, Office of Basic Energy Sciences under Award No. DE-SC0001004. TT prepared and handled the samples, and contributed to the processing and analysis of DNP-NMR data, with support from the U.S. National Science Foundation (NSF), Award No. CHE-1800596. Initial sample preparation and handling by LL were supported by funding from the U.S. Department of Energy, Office of Science, Division of Basic Energy Sciences, under the Catalysis Science Initiative (DE-FG-02-03ER15467). The experiments made use of the MRL Shared Experimental Facilities, supported by the MRSEC Program of the NSF under Award No. DMR-1720256.

Notes

The authors declare no competing financial interest.

ACKNOWLEDGMENTS

Scheme 2 was provided by Dr. Prashant Kumar.

REFERENCES

(1) Muraza, O.; Galadima, A. Isomerization and Alkylation of Biomass-Derived Compounds in Aqueous Media over Hydrophobic Solid Acid Catalysts: A Mini Review. *Ind. Eng. Chem. Res* **2014**, *53*, 17869–17877.

(2) Qi, L.; Alamillo, R.; Elliott, W. A.; Andersen, A.; Hoyt, D. W.; Walter, E. D.; Han, K. S.; Washton, N. M.; Rioux, R. M.; Dumesic, J. A.; Scott, S. L. Operando Solid-State NMR Observation of Solvent-Mediated Adsorption-Reaction of Carbohydrates in Zeolites. *ACS Catal.* **2017**, *7*, 3489–3500.

(3) Caeiro, G.; Magnoux, P.; Lopes, J. M.; Ribeiro, F. R.; Menezes, S. M. C.; Costa, A. F.; Cerqueira, H. S. Stabilization Effect of Phosphorus on Steamed H-MFI Zeolites. *Appl. Catal., A* **2006**, *314*, 160–171.

(4) Prinsloo, N. M. Solid Phosphoric Acid Oligomerisation: Manipulating Diesel Selectivity by Controlling Catalyst Hydration. *Fuel Process. Technol.* **2006**, *87*, 437–442.

(5) Cavani, F.; Girotti, G.; Terzoni, G. Effect of Water in the Performance of the "Solid Phosphoric Acid" Catalyst for Alkylation of Benzene to Cumene and for Oligomerization of Propene. *Appl. Cata. A-Gen.* **1993**, *97*, 177–196.

(6) Zhang, J.; Yan, Y.; Chu, Q.; Feng, J. Solid Phosphoric Acid Catalyst for Propene Oligomerization: Effect of Silicon Phosphate Composition. *Fuel Process. Technol.* **2015**, *135*, 2–5.

(7) Zhang, Z.; Lu, Q.; Ye, X.; Wang, T.; Wang, X.; Dong, C. Selective Production of Levoglucosenone from Catalytic Fast Pyrolysis of Biomass Mechanically Mixed with Solid Phosphoric Acid Catalysts. *Bioenerg. Res.* **2015**, *8*, 1263–1274.

(8) Santander, J. A.; Alvarez, M.; Gutierrez, V.; Volpe, M. A. Solid Phosphoric Acid Catalysts Based on Mesoporous Silica for Levoglucosenone Production via Cellulose Fast Pyrolysis. *J. Chem. Technol. Biotechnol.* **2019**, *94*, 484–493.

(9) Blasco, T.; Corma, A.; Martínez-Triguero, J. Hydrothermal Stabilization of ZSM-5 Catalytic-Cracking Additives by Phosphorus Addition. *J. Catal.* **2006**, *237*, 267–277.

(10) Rahimi, N.; Karimzadeh, R. Catalytic Cracking of Hydrocarbons over Modified ZSM-5 Zeolites to Produce Light Olefins: A Review. *Appl. Catal., A* **2011**, *398*, 1–17.

(11) Ding, J.; Wang, M.; Peng, L.; Xue, N.; Wang, Y.; He, M.-Y. Combined Desilication and Phosphorus Modification for High-Silica ZSM-5 Zeolite with Related Study of Hydrocarbon Cracking Performance. *Appl. Catal. A: Gen.* **2015**, *503*, 147–155.

(12) Altynkovich, E. O.; Potapenko, O. V.; Sorokina, T. P.; Doronin, V. P.; Gulyaeva, T. I.; Talzi, V. P. Butane–Butylene Fraction Cracking over Modified ZSM-5 Zeolite. *Pet. Chem.* **2017**, *57*, 215–221.

(13) Xue, N.; Chen, X.; Nie, L.; Guo, X.; Ding, W.; Chen, Y.; Gu, M.; Xie, Z. Understanding the Enhancement of Catalytic Performance for Olefin Cracking: Hydrothermally Stable Acids in P/HZSM-5. *J. Catal.* **2007**, *248*, 20–28.

(14) Cho, H. J.; Ren, L.; Vattipalli, V.; Yeh, Y.-H.; Gould, N.; Xu, B.; Gorte, R. J.; Lobo, R.; Dauenhauer, P. J.; Tsapatsis, M.; Fan, W. Renewable *p* -Xylene from 2,5-Dimethylfuran and Ethylene Using Phosphorus-Containing Zeolite Catalysts. *ChemCatChem* **2017**, *9*, 398–402.

(15) Abdelrahman, O. A.; Park, D. S.; Vinter, K. P.; Spanjers, C. S.; Ren, L.; Cho, H. J.; Vlachos, D. G.; Fan, W.; Tsapatsis, M.; Dauenhauer, P. J. Biomass-Derived Butadiene by Dehydra-Decyclization of Tetrahydrofuran. *ACS Sustain. Chem. Eng.* **2017**, *5*, 3732–3736.

(16) Lercher, J. A.; Rumplmayr, G. Controlled Decrease of Acid Strength by Orthophosphoric Acid on ZSM5. *Appl. Catal.* **1986**, *25*, 215–222.

(17) Wang, X.; Li, W.; Harrington, R.; Liu, F.; Parise, J. B.; Feng, X.; Sparks, D. L. Effect of Ferrihydrite Crystallite Size on Phosphate Adsorption Reactivity. *Environ. Sci. Technol.* **2013**, *47*, 10322–10331.
(18) Wang, X.; Hu, Y.; Tang, Y.; Yang, P.; Feng, X.; Xu, W.; Zhu, M. Phosphate and Phytate Adsorption and Precipitation on Ferrihydrite Surfaces. *Environ. Sci. Technol.* **2017**, *4*, 2193–2204.
(19) Wang, X.; Phillips, B. L.; Boily, J.-F.; Hu, Y.; Hu, Z.; Yang, P.; Feng, X.; Xu, W.; Zhu, M. Phosphate Sorption Speciation and Precipitation Mechanisms on Amorphous Aluminum Hydroxide. *Soil Syst.* **2019**, *3*, 20.
(20) van der Bij, H. E.; Weckhuysen, B. M. Phosphorus Promotion and Poisoning in Zeolite-Based Materials: Synthesis, Characterisation and Catalysis. *Chem. Soc. Rev.* **2015**, *44*, 7406–7428.
(21) Busca, G.; Ramis, G.; Lorenzelli, V.; Rossi, P. F.; La Ginestra, A.; Patrono, P. Phosphoric Acid on Oxide Carriers. 1. Characterization of Silica, Alumina, and Titania Impregnated by Phosphoric Acid. *Langmuir* **1989**, *5*, 911–916.
(22) Abdelghany, A. M.; Zeyada, H. M.; ElBatal, H. A.; Fetouh, R. Synthesis and Spectral Properties of Nd_2O_3-Doped Sodium Silicophosphate Glass. *Silicon* **2016**, *8*, 325–330.
(23) Ahsan, M. R.; Uddin, M. A.; Mortuza, M. G. Infrared Study of the Effect of P_2O_5 in the Structure of Lead Silicate Glasses. *Appl. Phys.* **2005**, *43*, 11.
(24) Kosinski, S. G.; Krol, D. M.; Duncan, T. M.; Douglas, D. C.; MacChesney, J. B.; Simpson, J. R. Raman and NMR Spectroscopy of SiO_2 Glasses CO-Doped with Al_2O_3 and P_2O_5. *J. Non. Cryst. Solids* **1988**, *105*, 45–52.
(25) Shibata, N.; Horigudhi, M.; Edahiro, T. Raman Spectra of Binary High-Silica Glasses and Fibers Containing GeO_2, P_2O_5 and B_2O_3. *J. Non. Cryst. Solids* **1981**, *45*, 115–126.
(26) Wan, B.; Huang, R.; Diaz, J. M.; Tang, Y. Polyphosphate Adsorption and Hydrolysis on Aluminum Oxides. *Environ. Sci. Technol.* **2019**, *53*, 9542–9552.
(27) Li, D.; Fleet, M. E.; Bancroft, G. M.; Kasrai, M.; Pan, Y. Local Structure of Si and P in SiO_2–P_2O_5 and Na_2O–SiO_2–P_2O_5 Glasses: A XANES Study. *J. Non. Cryst. Solids* **1995**, *188*, 181–189.
(28) Liu, Z.; Chen, Z.-X.; Ding, W.; Kang, G.-J.; Li, Z. A Density Functional Study of Pentacoordinated Phosphorus Species in ZSM-5 Zeolite. *J Mol. Struc.-theochem* **2010**, *948*, 99–101.
(29) Sastre, G.; Lewis, D. W.; Catlow, C. R. A. Structure and Stability of Silica Species in SAPO Molecular Sieves. *J. Phys. Chem.* **1996**, *100*, 6722–6730.
(30) Aronne, A.; Turco, M.; Bagnasco, G.; Pernice, P.; Di Serio, M.; Clayden, N. J.; Marenna, E.; Fanelli, E. Synthesis of High Surface Area Phosphosilicate Glasses by a Modified Sol–Gel Method. *Chem. Mater.* **2005**, *17*, 2081–2090.
(31) Clayden, N. J.; Esposito, S.; Pernice, P.; Aronne, A. Solid State ^{29}Si and ^{31}P NMR Study of Gel Derived Phosphosilicate Glasses. *J. Mater. Chem.* **2001**, *11*, 936–943.
(32) Coelho, C.; Azais, T.; Bonhomme-Coury, L.; Maquet, J.; Massiot, D.; Bonhomme, C. Application of the MAS-J-HMQC Experiment to a New Pair of Nuclei $\{^{29}Si,^{31}P\}$: $Si_5O(PO_4)_6$ and SiP_2O_7 Polymorphs. *J. Magn. Reson.* **2006**, *179*, 114–119.
(33) Krawietz, T. R.; Lin, P.; Lotterhos, K. E.; Torres, P. D.; Barich, D. H.; Clearfield, A.; Haw, J. F. Solid Phosphoric Acid Catalyst: A Multinuclear NMR and Theoretical Study. *J. Am. Chem. Soc.* **1998**, *120*, 8502–8511.
(34) Huhti, A.-L.; Gartaganis, P. A. The Composition of the Strong Phosphoric Acids. *Can. J. Chem.* **1956**, *34*, 785–797.
(35) Jameson, R. F. The Composition of the "Strong" Phosphoric Acids. *J. Chem. Soc.* **1959**, 752–759.
(36) Prinsloo, N. M. Preparation of a Solid Phosphoric Acid Catalyst from Low-Quality Kieselguhr Parameters Controlling Catalyst Quality and Performance. *Ind. Eng. Chem. Res.* **2007**, *46*, 7838–7843.
(37) de Klerk, A.; Leckel, D. O.; Prinsloo, N. M. Butene Oligomerization by Phosphoric Acid Catalysis: Separating the Effects of Temperature and Catalyst Hydration on Product Selectivity. *Ind. Eng. Chem. Res.* **2006**, *45*, 6127–6136.
(38) Villa, M.; Scagliotti, M.; Chiodelli, G. Short Range Order in the Network of the Borophosphate Glasses: A ^{31}P NMR-MAS (Magic Angle Spinning) Study. *J. Non-Cryst. Solids* **1987**, *94*, 101–121.
(39) Jeschke, G.; Hoffbauer, W.; Jansen, M. Survival of Dipolar Splittings between Equivalent Nuclei in High-Speed MAS-NMR—Interpretation of the ^{31}P Coupling Patterns for Tetraphosphorus Decaoxide. *Chem. - Eur. J.* **1998**, *4*, 1755–1761.
(40) Szu, S.-P.; Klein, L. C.; Greenblatt, M. Effect of Precursors on the Structure of Phosphosilicate Gels: ^{29}Si and ^{31}P MAS-NMR Study. *J. Non-Cryst. Solids* **1992**, *143*, 21–30.
(41) Coelho, C.; Babonneau, F.; Azaïs, T.; Bonhomme-Coury, L.; Maquet, J.; Laurent, G.; Bonhomme, C. Chemical Bonding in Silicophosphate Gels: Contribution of Dipolar and J-Derived Solid State NMR Techniques. *J. Sol-Gel Sci. Technol.* **2006**, *40*, 181–189.
(42) Wang, L.; Samuels, W. D.; Exarhos, G. J.; Lee, B. I.; Cao, Z. ^{31}P and ^{29}Si NMR Study of Sol–Gel-Synthesized Phosphate Ceramics. *J. Mater. Chem.* **1998**, *8*, 165–169.
(43) Mudrakovskii, I. L.; Mastikhin, V. M.; Shmachkova, V. P.; Kotsarenko, N. S. High-Resolution Solid-State ^{29}Si and ^{31}P NMR of Silicon-Phosphorous Compounds Containing Six-Coordinated Silicon. *Chem. Phys. Lett.* **1985**, *120*, 424–426.
(44) García, A.; Colilla, M.; Izquierdo-Barba, I.; Vallet-Regí, M. Incorporation of Phosphorus into Mesostructured Silicas: A Novel Approach to Reduce the SiO_2 Leaching in Water. *Chem. Mater.* **2009**, *21*, 4135–4145.
(45) Das, S. K.; Bhunia, M. K.; Chakraborty, D.; Khuda-Bukhsh, A. R.; Bhaumik, A. Hollow Spherical Mesoporous Phosphosilicate Nanoparticles as a Delivery Vehicle for an Antibiotic Drug. *Chem. Comm.* **2012**, *48*, 2891–2893.
(46) Hartmann, P.; Jana, C.; Vogel, J.; Jäger, C. ^{31}P MAS and 2D Exchange NMR of Crystalline Silicon Phosphates. *Chem. Phys. Lett.* **1996**, *258*, 107–112.
(47) Grimmer, A.-R.; Haubenreisser, U. High-Field Static and MAS ^{31}P NMR: Chemical Shift Tensors of Polycrystalline Potassium Phosphates $P_2O_5{\cdot}xK_2O$ ($O \leq x \leq 3$). *Chem. Phys. Lett.* **1983**, *99*, 487–490.
(48) Tropp, J.; Blumenthal, N. C.; Waugh, J. S. Phosphorus NMR Study of Solid Amorphous Calcium Phosphate. *J. Am. Chem. Soc.* **1983**, *105*, 22–26.
(49) Coelho, C.; Azaïs, T.; Bonhomme-Coury, L.; Laurent, G.; Bonhomme, C. Efficiency of the Refocused ^{31}P–^{29}Si MAS-J-INEPT NMR Experiment for the Characterization of Silicophosphate Crystalline Phases and Amorphous Gels. *Inorg. Chem.* **2007**, *46*, 1379–1387.
(50) Fayon, F.; King, I. J.; Harris, R. K.; Evans, J. S. O.; Massiot, D. Application of the Through-Bond Correlation NMR Experiment to the Characterization of Crystalline and Disordered Phosphates. *C. R. Chim.* **2004**, *7*, 351–361.
(51) O'Dell, L. A.; Guerry, P.; Wong, A.; Abou Neel, E. A.; Pham, T. N.; Knowles, J. C.; Brown, S. P.; Smith, M. E. Quantification of Crystalline Phases and Measurement of Phosphate Chain Lengths in a Mixed Phase Sample by ^{31}P Refocused INADEQUATE MAS NMR. *Chem. Phys. Lett.* **2008**, *455*, 178–183.
(52) J. King, I.; Fayon, F.; Massiot, D.; K. Harris, R.; O. Evans, J. S. A Space Group Assignment of ZrP_2O_7 Obtained by ^{31}P Solid State NMR. *Chem. Comm.* **2001**, *0*, 1766–1767.
(53) Helluy, X.; Marichal, C.; Sebald, A. Through-Bond Indirect and Through-Space Direct Dipolar Coupling ^{31} P MAS NMR Constraints for Spectral Assignment in the Cubic $3 \times 3 \times 3$ Superstructure of TiP_2O_7. *J. Phys. Chem. B* **2000**, *104*, 2836–2845.
(54) Lilly Thankamony, A. S.; Wittmann, J. J.; Kaushik, M.; Corzilius, B. Dynamic Nuclear Polarization for Sensitivity Enhancement in Modern Solid-State NMR. *Prog. Nucl. Magn. Reson. Spectrosc.* **2017**, *102–103*, 120–195.
(55) Zhang, X.; Liu, D.; Xu, D.; Asahina, S.; Cychosz, K. A.; Agrawal, K. V.; Wahedi, Y. A.; Bhan, A.; Hashimi, S. A.; Terasaki, O.; Thommes, M.; Tsapatsis, M. Synthesis of Self-Pillared Zeolite Nanosheets by Repetitive Branching. *Science* **2012**, *336*, 1684–1687.

(56) Guefrachi, Y.; Sharma, G.; Xu, D.; Kumar, G.; Vinter, K. P.; Abdelrahman, O. A.; Li, X.; Alhassan, S.; Dauenhauer, P. J.; Navrotsky, A.; Zhang, W.; Tsapatsis, M. Steam-Induced Coarsening of Single-Unit-Cell MFI Zeolite Nanosheets and Its Effect on External Surface Brønsted Acid Catalysis. *Angew. Chem. Int. Ed.* **2020**, *59*, 9579–9585.
(57) Norton, A. M.; Kim, D.; Zheng, W.; Akter, N.; Xu, Y.; Tenney, S. A.; Vlachos, D. G.; Tsapatsis, M.; Boscoboinik, J. A. Reversible Formation of Silanol Groups in Two-Dimensional Siliceous Nanomaterials under Mild Hydrothermal Conditions. *J. Phys. Chem. C* **2020**, *124*, 18045–18053.
(58) Coetzee, J. H.; Mashapa, T. N.; Prinsloo, N. M.; Rademan, J. D. An Improved Solid Phosphoric Acid Catalyst for Alkene Oligomerization in a Fischer–Tropsch Refinery. *Appl. Catal., A* **2006**, *308*, 204–209.
(59) van der Bij, H. E.; Weckhuysen, B. M. Phosphorus Promotion and Poisoning in Zeolite-Based Materials: Synthesis, Characterisation and Catalysis. *Chem. Soc. Rev.* **2015**, *44*, 7406–7428.
(60) Jain, S.; Bjerring, M.; Nielsen, N. C. Efficient and Robust Heteronuclear Cross-Polarization for High-Speed-Spinning Biological Solid-State NMR Spectroscopy. *J. Phys. Chem. Lett.* **2012**, *3*, 703–708.
(61) Mulliken, R. S. The Interaction of Electron Donors and Acceptors. *J. Chim. Phys.* **1964**, *61*, 20–38.
(62) Reed, A. E.; Curtiss, L. A.; Weinhold, F. Intermolecular Interactions from a Natural Bond Orbital, Donor-Acceptor Viewpoint. *Chem. Rev.* **1988**, *88*, 899–926.
(63) Timoneda, J. I.; Hynes, J. T. Nonequilibrium Free Energy Surfaces for Hydrogen-Bonded Proton-Transfer Complexes in Solution. *J. Phys. Chem.* **1991**, *95*, 10431–10442.
(64) Thompson, W. H.; Hynes, J. T. Model Study of the Acid–Base Proton-Transfer Reaction of the ClH···OH_2 Pair in Low-Polarity Solvents. *J. Phys. Chem. A* **2001**, *105*, 2582–2590.
(65) Ratajczak, H. Charge-Transfer Properties of the Hydrogen Bond. I. Theory of the Enhancement of Dipole Moment of Hydrogen-Bonded Systems. *J. Phys. Chem.* **1972**, *76*, 3000–3004.
(66) Warshel, A. Dynamics of Enzymatic Reactions. *Proc. Natl. Acad. Sci. U. S. A.* **1984**, *81*, 444–448.
(67) Warshel, Arieh.; Russell, Stephen. Theoretical Correlation of Structure and Energetics in the Catalytic Reaction of Trypsin. *J. Am. Chem. Soc.* **1986**, *108*, 6569–6579.
(68) Warshel, A.; Weiss, R. M. An Empirical Valence Bond Approach for Comparing Reactions in Solutions and in Enzymes. *J. Am. Chem. Soc.* **1980**, *102*, 6218–6226.
(69) Warshel, A. Dynamics of Reactions in Polar Solvents. Semiclassical Trajectory Studies of Electron-Transfer and Proton-Transfer Reactions. *J. Phys. Chem.* **1982**, *86*, 2218–2224.
(70) Harris, N.; Wei, W.; Saunders, W. H.; Shaik, S. Origins of Nonperfect Synchronization in the Lowest-Energy Path of Identity Proton Transfer Reactions Leading to Delocalized Anions: A VBSCF Study[1]. *J. Am. Chem. Soc.* **2000**, *122*, 6754–6758.
(71) Wu, W.; Shaik, S.; Saunders, W. H. Comparative Study of Identity Proton-Transfer Reactions between Simple Atoms or Groups by VB Methods. *J. Phys. Chem. A* **2002**, *106*, 11616–11622.
(72) Keeffe, J. R.; Gronert, S.; Colvin, M. E.; Tran, N. L. Identity Proton-Transfer Reactions from C–H, N–H, and O–H Acids. An Ab Initio, DFT, and CPCM-B3LYP Aqueous Solvent Model Study. *J. Am. Chem. Soc.* **2003**, *125*, 11730–11745.
(73) Irani, R. R.; Callis, C. F. Metal Complexing by Phosphorus Compounds. IV. Acidity Constants. *J. Phys. Chem.* **1961**, *65*, 934–937.
(74) Lejeune, C.; Coelho, C.; Bonhomme-Coury, L.; Azaïs, T.; Maquet, J.; Bonhomme, C. Studies of Silicophosphate Derivatives by $^{31}P \rightarrow {}^{29}Si$ CP MAS NMR. *Solid State Nucl. Magn. Reson.* **2005**, *27*, 242–246.
(75) Schaefer, J.; McKay, R. A.; Stejskal, E. O. Double-Cross-Polarization NMR of Solids. *J. Magn. Reson.* **1979**, *34*, 443–447.
(76) Bennett, A. E.; Rienstra, C. M.; Griffiths, J. M.; Zhen, W.; Lansbury, P. T.; Griffin, R. G. Homonuclear Radio Frequency-Driven Recoupling in Rotating Solids. *J. Chem. Phys.* **1998**, *108*, 9463–9479.
(77) Feike, M.; Jäger, C.; Spiess, H. W. Connectivities of Coordination Polyhedra in Phosphate Glasses from ^{31}P Double-Quantum NMR Spectroscopy. *J. Non-Cryst. Solids* **1998**, *223*, 200–206.
(78) Hohwy, M.; Rienstra, C. M.; Jaroniec, C. P.; Griffin, R. G. Fivefold Symmetric Homonuclear Dipolar Recoupling in Rotating Solids: Application to Double Quantum Spectroscopy. *J. Chem. Phys.* **1999**, *110*, 7983–7992.
(79) Williams, D. B. G.; Lawton, M. Drying of Organic Solvents: Quantitative Evaluation of the Efficiency of Several Desiccants. *J. Org. Chem.* **2010**, *75*, 8351–8354.
(80) Mehring, M. *Principles of High Resolution NMR in Solids*, 2nd ed.; Springer-Verlag: Berlin Heidelberg, 1983.
(81) Hediger, S.; Meier, B. H.; Ernst, R. R. Adiabatic Passage Hartmann-Hahn Cross Polarization in NMR under Magic Angle Sample Spinning. *Chem.Phys. Lett.* **1995**, *240*, 449–456.
(82) Bak, M.; Rasmussen, J. T.; Nielsen, N. C. SIMPSON: A General Simulation Program for Solid-State NMR Spectroscopy. *J. Magn. Reson.* **2011**, *213*, 366–400.
(83) Frisch, M. J.; Trucks, G. W.; Schlegel, H. B.; Scuseria, G. E.; Robb, M. A.; Cheeseman, J. R.; Scalmani, G.; Barone, V.; Mennucci, B.; Petersson, G. A.; Nakatsuji, H.; Caricato, M.; Li, X.; Hratchian, H. P.; Izmaylov, A. F.; Bloino, J.; Zheng, G.; Sonnenberg, J. L.; Hada, M.; Ehara, M.; Toyota, K.; Fukuda, R.; Hasegawa, J.; Ishida, M.; Nakajima, T.; Honda, Y.; Kitao, O.; Nakai, H.; Vreven, T.; Montgomery Jr., J. A.; Peralta, J. E.; Ogliaro, F.; Bearpark, M. J.; Heyd, J.; Brothers, E. N.; Kudin, K. N.; Staroverov, V. N.; Kobayashi, R.; Normand, J.; Raghavachari, K.; Rendell, A. P.; Burant, J. C.; Iyengar, S. S.; Tomasi, J.; Cossi, M.; Rega, N.; Millam, N. J.; Klene, M.; Knox, J. E.; Cross, J. B.; Bakken, V.; Adamo, C.; Jaramillo, J.; Gomperts, R.; Stratmann, R. E.; Yazyev, O.; Austin, A. J.; Cammi, R.; Pomelli, C.; Ochterski, J. W.; Martin, R. L.; Morokuma, K.; Zakrzewski, V. G.; Voth, G. A.; Salvador, P.; Dannenberg, J. J.; Dapprich, S.; Daniels, A. D.; Farkas, Ö.; Foresman, J. B.; Ortiz, J. V; Cioslowski, J.; Fox, D. J. Gaussian 09. Gaussian, Inc.: Wallingford, CT, USA 2009.

Table of Contents artwork